

Fiber-based polarization-sensitive Fourier domain
optical coherence tomography

Masahiro Yamanari
(Doctoral Program in Applied Physics)

Submitted to the Graduate School of
Pure and Applied Sciences
in Partial Fulfillment of the Requirements
for the Degree of Doctor of Philosophy in
Engineering

at the
University of Tsukuba

Contents

Abstract of dissertation	1
1 Introduction	3
2 Fiber-based polarization-sensitive spectral-domain optical coherence tomography	7
Abstract	7
2.1 The optical system and the synchronization system	8
2.1.1 Overview	8
2.1.2 Calibration of the polarization-sensitive spectrometer	8
2.2 Theory	10
2.2.1 The Jones matrix imaging method using polarization modulation method along lateral B-scan	10
2.2.2 Compensation of the fiber-induced birefringence	13
2.2.3 Discrete polarization modulation	13
2.3 Experimental results and discussion	14
2.3.1 Measurements of a polarizer and a waveplate	14
2.3.2 Measurements of biological samples	14
2.4 Summary	18
3 Application of PS-SD-OCT for the phase retardation measurement of retinal nerve fiber layer	21
Abstract	21
3.1 Introduction	22
3.2 Methods	23
3.2.1 PS-SD-OCT system	23
3.2.2 Three-dimensional volumetric measurement by PS-SD-OCT	23
3.2.3 <i>En face</i> phase retardation maps	24
3.2.4 Quantitative analysis of phase retardation	26
3.3 Results and discussion	26
3.3.1 Subjects	26

3.3.2	Three-dimensional phase retardation volume	26
3.3.3	Healthy eye	29
3.3.4	Glaucomatous eye	30
3.3.5	Observation of the phase retardation by polar plot	35
3.4	Summary	37
4	Fiber-based polarization-sensitive swept-source optical coherence tomography	39
	Abstract	39
4.1	Introduction	40
4.2	System and theory	40
	4.2.1 System configuration	40
	4.2.2 Principle of polarization-sensitive detection	41
	4.2.3 Calibration of phase fluctuation	46
4.3	Results	48
	4.3.1 Measurements of a quarter-wave plate and linear polarizer	48
	4.3.2 Measurements of biological samples	50
4.4	Discussion	51
4.5	Summary	53
5	Conclusion	55
	Bibliography	57
	Acknowledgements	65
	Curriculum vitae	67

List of Figures

2.1	Diagram of the PS-SD-OCT system.	9
2.2	Depth-dependent phase difference of the OCT signals between horizontal and vertical channels.	10
2.3	Measured orientations of LP and QWP, and measured phase retardation of QWP.	15
2.4	Intensity, phase retardation and orientation images of chicken breast muscle.	16
2.5	Images of chicken breast muscle with different modulations.	17
2.6	Intensity, phase retardation and orientation images of a finger pad.	17
2.7	Intensity and phase retardation images of caries lesion of human canine tooth.	18
3.1	Diagram of the PS-SD-OCT system for the retinal imaging.	23
3.2	Intensity, phase retardation images of inferior of an optic nerve head of a healthy human left eye.	25
3.3	Three-dimensional phase retardation image of a healthy eye in the peripheral region.	27
3.4	The phase retardation maps of the healthy eye and glaucomatous eye on the surface of retina.	28
3.5	The histograms of the phase retardation of the healthy eye and glaucomatous eye on the surface of retina.	28
3.6	Fundus image, nerve fiber thickness map measured by GDx-VCC, <i>en face</i> projection image of the OCT intensity, and <i>en face</i> phase retardation image measured by the PS-SD-OCT for the healthy eye.	29
3.7	Round-trip cumulative phase retardation around the optic nerve head of the healthy eye measured by PS-SD-OCT and GDx-VCC.	31
3.8	The thickness and DPPR/UD of RNFL of the healthy eye in the annular area.	32
3.9	Visual field test of the glaucomatous eye measured using the Humphrey field analyzer II	32
3.10	Fundus image, nerve fiber thickness map measured by GDx-VCC, <i>en face</i> projection image of the OCT intensity, and <i>en face</i> phase retardation image measured by the PS-SD-OCT for the glaucomatous eye.	33
3.11	Round-trip cumulative phase retardation around the optic nerve head of the glaucomatous eye measured by PS-SD-OCT and GDx-VCC.	34

3.12	OCT B-scan images of a glaucomatous eye in the superior and inferior regions.	35
3.13	The thickness and DPPR/UD of RNFL of the glaucomatous eye in the annular area.	36
3.14	Polar plot of the TSNIT phase retardation curve over the <i>en face</i> phase retardation map of the healthy eye.	37
3.15	Polar plot of the TSNIT phase retardation curve over the <i>en face</i> phase retardation map of the glaucomatous eye.	38
4.1	Schematic of the PS-SS-OCT system.	42
4.2	Diagram of the detected signal after Fourier transform.	45
4.3	Flowchart of the data processing.	49
4.4	Double-pass phase retardation of the QWP, double-pass diattenuation of the LP, and relative orientation of the QWP and LP.	50
4.5	Intensity, phase retardation and orientation images of the chicken breast muscle.	51
4.6	Intensity, phase retardation and orientation images of the <i>in vivo</i> human anterior eye segment.	52

List of Tables

1.1	Typical approaches of PS-OCT.	5
-----	---------------------------------------	---

Abstract of dissertation

Optical coherence tomography (OCT) has been developed to measure depth-resolved images of various biological tissues. Polarization-sensitive optical coherence tomography (PS-OCT) is a functional extension of OCT to measure the depth-resolved birefringence of biological fibrous tissues. PS-OCT with fiber-optic components is convenient to build it with probing scanners, e.g., fundus cameras and endoscopic scanners, but it requires additional complexities for the measurement and the data processing due to the unpredictable birefringence of the fiber-optic components. We have to measure depth-resolved Jones matrices of the sample to compensate the birefringence of the fiber-optic components, and it requires multiple depth scans for a single position on the sample in order to use multiple incident states of the polarization. Spectral-domain and swept-source OCT have been developed in recent years to improve the sensitivity and the resultant imaging speed over conventional time-domain OCT. The purpose of this study is to develop spectral domain and swept-source PS-OCT.

Fiber-based polarization-sensitive spectral-domain OCT (PS-SD-OCT) is developed at 840 nm wavelength. A polarization-sensitive spectrometer with two line-CCD cameras was developed for the PS-SD-OCT. The algorithm for the measurement is explained using the Jones matrix formalism. Three-dimensional intensity, phase retardation, and relative orientation images of the sample are measured for the demonstration.

As the application of the PS-SD-OCT, three-dimensional *in vivo* retinal nerve fiber layer (RNFL) is measured. For the first time, we compare the phase retardation of RNFL measured by PS-OCT and scanning laser polarimetry. The *en face* phase retardation maps are analyzed. We show that similar results are obtained using these systems for healthy and glaucomatous eyes.

The PS-SD-OCT had a restriction of transversal scanning density. We show the polarization-sensitive swept-source OCT (PS-SS-OCT) system at 1.3 μm which can measure birefringence of the sample with a single wavelength scan. The incident polarization is modulated at one-third of the frequency of the data acquisition. It generates frequency-shifted OCT signals with respect to the modulation frequency. Since this method can provide the Jones matrix of the sample with a single wavelength-scan, a highly dense scan is not required. We show the phase retardation image of anterior eye segment, which would give an additional information to discriminate fibrous tissue from other tissues.

Chapter 1

Introduction

Optical coherence tomography (OCT) is an interferometric imaging technique for the non-invasive measurement of biological samples [1]. Recent developments in Fourier-domain (FD) OCT, which involves spectral-domain (SD) and swept-source (SS) OCT, have dramatically improved the sensitivity [2–4]. Subsequently, high-speed OCT systems have been demonstrated [5–9]. Nowadays SD-OCT and SS-OCT are mainly used as the OCT engines instead of conventional time-domain (TD) OCT.

As a functional extension of OCT, polarization-sensitive OCT (PS-OCT) has been developed to measure the depth-resolved birefringence of biological tissues [10, 11]. PS-OCT has a unique and powerful characteristic to detect and analyze fibrous tissues, e.g., retinal nerve fiber layer [12–17], collagen fiber in skin [18–24] and cartilage [25], dentistry [26–30] and skeletal muscle [31].

Several methods and algorithms have been developed for PS-OCT. Free-space PS-OCT with a circularly polarized incident beam and polarization-sensitive detection is the simplest way to detect the phase retardation and orientation of the sample [32]. The Mueller matrix or Jones matrix represents complete polarimetric information of the sample, and they can be measured using several different states of the incident polarization [33, 34]. Yasuno et al. first implemented free-space PS-OCT with SD-OCT to measure the Mueller or Jones matrices of the sample [35, 36]. High-speed free-space PS-SD-OCT with a circularly polarized incident beam has been demonstrated by Göttinger et al. for retinal imaging [16]. To maintain the stable state of polarization in PS-OCT systems, the optical components have to be fixed mechanically. Therefore, free-space optical systems are more appropriate than optical-fiber-based systems. Although the calculation of birefringence becomes simple, the flexibility of the measurement, which is highly desired for medical examinations, is sacrificed.

In order to use fiber-optic components for PS-OCT, several algorithms have been developed, for example, the Stokes vector method [37], algebraic manipulation method with polarization-sensitive bulk optics in the sample arm [38], and Jones matrix method with sequential polarization modulation [39]. These methods require multiple depth scans with different incident

polarizations at the same position. This is because the first method needs to determine the rotating plane of the Stokes vectors on the Poincaré sphere, the second method needs to measure sufficient depth scans for algebraic manipulation, and the third method needs to measure all the complete four elements of a Jones matrix. Thus, a highly dense scan is necessary to maintain the correlation between adjacent axial scans. In the first and third methods, the motion of the sample poses a problem because it affects the signal phase.

In Chapter 2, we show our PS-SD-OCT system with B-scan-oriented polarization modulation. Fiber-optic components and a polarization-sensitive spectrometer are used for the optical setup. The incident polarized light is modulated along a lateral B-scan instead of an axial A-scan. The Jones matrix of the sample is obtained from the spatial frequencies of the B-scan. Fiber-induced birefringence is compensated by using the algorithm developed by Park et al. [39] Although this system requires highly dense transversal scan, we can measure various biological samples with high speed and high sensitivity. Chapter 3 is focused on the application of the PS-SD-OCT for the measurement of retinal nerve fiber layer (RNFL). For the first time, we compare the phase retardation of RNFL measured by PS-OCT and scanning laser polarimetry. The *en face* phase retardation maps are analyzed. We show that similar results are obtained using these systems for healthy and glaucomatous eyes.

To overcome the restriction of fiber-based PS-OCT, certain methods were developed and published by some groups. Jiao et al. developed fiber-based PS-OCT with two superposed light sources [40] and continuous polarization modulation [41] based on the time-domain OCT technique. Although fiber-based spectral-domain or swept-source PS-OCT was recently developed to achieve high sensitivity and resultant high imaging speed [42–46], only a system developed by Oh et al. [46] can measure birefringence of a sample with a single wavelength scan. The other fiber-based spectral-domain or swept-source PS-OCT systems alter the incident polarization for each depth scan and, therefore, require a highly dense scan.

In Chapter 4, we show our PS-SS-OCT system which can measure birefringence of the sample with a single wavelength scan. The incident polarization is modulated at one-third of the frequency of the data acquisition. It generates frequency-shifted OCT signals with respect to the modulation frequency. Since this method can provide the Jones matrix of the sample with a single wavelength-scan, a highly dense scan is not required. We show the phase retardation image of anterior eye segment, which would give an additional information to discriminate fibrous tissue from other tissues.

Table 1 summarizes typical approaches of PS-OCT including our systems described in Chapter 2 and 4.

Chapter 5 concludes this dissertation.

	Time domain		Fourier domain	
	Free space	Fiber-based	Free space	Fiber-based
A	Hee et al. [10] de Boer et al. [11] Hitzenberger et al. [32]		Göttinger et al. [16]	
B	de Boer et al. [47]	Saxer et al. [37]		Zhang et al. [42] Cense et al. [44] Oh et al. [46]
C		Roth et al. [38]		Zhao et al. [48]
D	Yao et al. [33]		Yasuno et al. [35]	
E	Jiao et al. [34]	Jiao et al. [40] Park et al. [39]	Yasuno et al. [36]	Park et al. [43]
F		Jiao et al. [41]		Yamanari et al. [45] Chapter 4

Table 1.1: Typical approaches of PS-OCT. A: circularly polarized incident light, B: Stokes vector, C: Algebraic manipulation, D: Mueller matrix, E: Jones matrix with two incident polarizations, F: Jones matrix with polarization modulation method.

Chapter 2

Fiber-based polarization-sensitive spectral-domain optical coherence tomography

Abstract

Fiber-based high-speed polarization-sensitive Fourier domain optical coherence tomography (PS-FD-OCT) with a probe wavelength of 840 nm is developed. This system uses a newly developed polarization modulation method. The incident state of polarization is modulated along transversal scanning (B-scan). The spectrometer has a polarizing beamsplitter and two line-CCD cameras operated at a line rate of 27.7 kHz. From the 0th and 1st orders of the spatial frequencies along the B-scanning, a depth-resolved Jones matrix can be derived. The first version of this system had been based on a continuous polarization modulation. However, this continuous polarization modulation along B-scan causes fringe washout. Equivalent discrete polarization modulation method which has been developed to avoid the problem of fringe-wash-out is applied to biological measurements. As a system demonstration, an *in vitro* chicken breast muscle, an *in vivo* finger pad, and an *in vivo* caries lesion of a human tooth are measured. Three dimensional phase retardation images show the potentials for applying the system to biological and medical studies.

2.1 The optical system and the synchronization system

2.1.1 Overview

The diagram of our system is shown in Fig. 2.1. The light source is a superluminescent diode (SLD-37-HP, Superlum, Russia) with a central wavelength of 840 nm, bandwidth of 50 nm, and axial resolution of $8.3 \mu\text{m}$ in air. After the polarization is vertically aligned by a linear polarizer (LP), an EO modulator (4104, New Focus, CA, USA) with a fast axis of 45° modulates the incident polarization. The modulated light is coupled into a 30/70 fiber coupler. 30% of the incident light is delivered into the sample arm, and 70% is delivered into the reference arm. This splitting ratio was selected for the future application of retinal measurement to conform to a safety standard of the illumination power. An LP is inserted in the reference arm to obtain constant amplitude and constant relative phase between the two orthogonal polarizations at the spectrometer independent of the incident state of the polarization. This configuration was achieved by an iterative alignment of the polarization controller and LP in the reference arm. In the sample arm, the 1.5 mm diameter beam focused by a 50 mm focal length lens is scanned by the two-axis galvanoscanner mirror. The probing power is $700 \mu\text{W}$. The theoretical transversal resolution and focal depth are $36 \mu\text{m}$ and 2.4 mm, respectively. The backscattered light from the sample goes through the fiber coupler again, and is detected by the spectrometer. In the spectrometer, the interfered beam is collimated with a 120 mm focal length lens, dispersed by a polarization-insensitive volume phase holographic grating of 1200 lines/mm (Wasatch Photonics, UT, USA), spatially Fourier transformed by a 250 mm focal length lens, divided into horizontally and vertically polarized components by a polarizing beamsplitter, and detected by two line-CCD cameras of 2048 pixels and $14 \mu\text{m}$ pixel size (AVIIVA M2 CL 2014, Atmel, CA, USA). A line trigger for both cameras (27.7 kHz) is generated by a DAQ board and synchronized with the galvanoscanner mirror in the sample arm and the EO modulator. The waveform driving the galvanoscanner mirror is a sawtooth wave, and that driving the EO modulator is a sinusoidal wave or a three-step function. The further details are described in Sec. 2.2. The data from both cameras are acquired by a framegrabber (PCIe-1430, National Instruments, TX, USA). The sensitivity of the system is 100.7 dB, which is obtained by adding the horizontal and vertical channels. The phase stability is 3.24 degrees at the signal-to-noise ratio of 27.6 dB, which is reasonably stable for this signal-to-noise ratio [43].

2.1.2 Calibration of the polarization-sensitive spectrometer

Since two line-CCD cameras are used to detect both phase-resolved horizontally and vertically polarized signals, these two cameras must construct two identical spectrometers. Park et al. explained the method of the calibration briefly [43]. Göttinger et al. derived the equations of the effect of the misalignment of the spectrometer [16]. Since the pixel size of our line-CCD cameras is smaller than that of previously reported $1.3 \mu\text{m}$ system [43], finer calibration is required. In this section, we describe our detailed method of the calibration. In order to

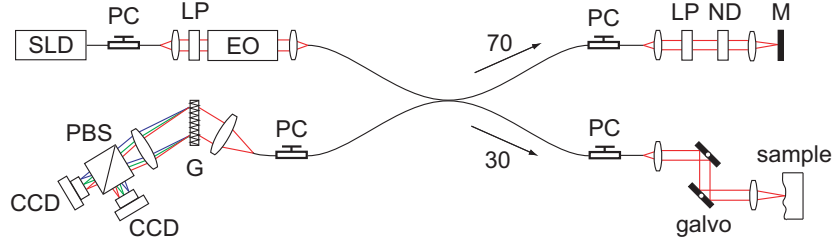


Figure 2.1: Diagram of the PS-SD-OCT system. The notations imply the following: SLD: superluminescent diode, PC: polarization controller, ND: neutral density filter, LP: linear polarizer, EO: electro-optic modulator, M: mirror, G: grating, PBS: polarizing beamsplitter, CCD: line-CCD camera.

calibrate these two spectrometers, the EO modulation is stopped. The reference light is blocked, and a slide glass and mirror are placed in the sample arm. This configuration ensures that the positions of the peak are the same for the horizontal and vertical channels. If both the reference and sample arms are used for the calibration in the fiber-based system, random birefringence of the reference and the sample arms causes a random phase difference between the horizontally and vertically polarized components of the OCT signals detected by these two spectrometers. Since the position of the fiber can easily change during the calibration, it is efficient to use only one arm of the interferometer. The OCT signals from the back surface of the glass and mirror are obtained for these two spectrometers. The phase difference at the peak of the OCT signals is monitored. This phase difference should be zero for all axial depths. In addition, the signals are windowed and inverse Fourier transformed to obtain the complex spectrum for the two spectrometers. This spectral phase difference is also monitored because it should be zero for all frequencies. By monitoring these values, the physical positions of the two cameras are aligned to minimize the phase difference. Since fine calibration is needed, both the cameras are mounted on the translation stages including the $XYZ\theta\alpha$ axes, where XYZ are the axes of Cartesian coordinates (X and Y are parallel and perpendicular to the line-CCD, respectively, and Z is the height); θ , a tilt of the line-CCD on the XY plane; and α , a tilt on the XZ plane. The optical table on which the spectrometer is built should be rigid, and air fluctuation should be avoided. After the physical calibration, the remaining difference is numerically compensated by adjusting the 0th and 1st order coefficients of the wavelength-frequency rescaling parameters. To verify the calibration, we measured OCT signals between the slide glass and mirror at different axial depth. Figure 2.2 represents the phase difference between the OCT signals from two channels with respect to the axial depth. The phase difference is within ± 4 deg for all axial depths.

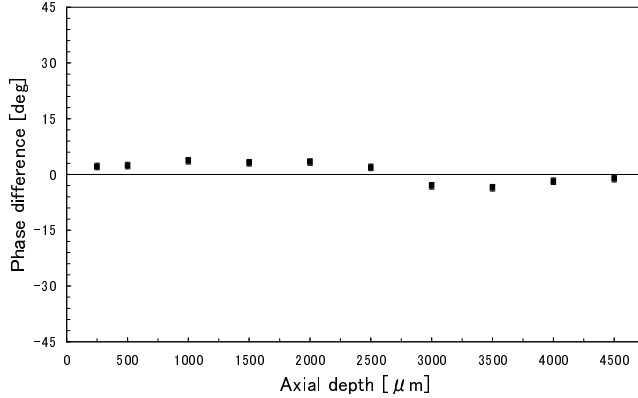


Figure 2.2: Depth-dependent phase difference of the OCT signals between horizontal and vertical channels. The interference signal is generated by the back surface of the slide glass and the mirror.

2.2 Theory

In this section, we describe our algorithm and the calibration method used to obtain a Jones matrix OCT image.

2.2.1 The Jones matrix imaging method using polarization modulation method along lateral B-scan

We denote the horizontally polarized component of the intensity of the interfered light at the spectrometer as I_h . It can be expressed as

$$I_h(x, \omega) = |H_{ref}(x, \omega)|^2 + |H_{sam}(x, \omega)|^2 + H_{ref}(x, \omega)H_{sam}^*(x, \omega) + c.c., \quad (2.1)$$

where $H_{ref}(x, \omega)$ and $H_{sam}(x, \omega)$ are the horizontally polarized temporal spectral components of the reference beam and sample beam, respectively, and c.c. denotes the complex conjugate of the third term on the right-hand-side of Eq. (2.1). The superscript * denotes the complex conjugate, and ω is the optical frequency. The third term in Eq. (2.1) is extracted and inverse Fourier transformed to obtain the complex OCT signal,

$$\tilde{I}_h(x, z) = \mathcal{F}_{z\omega}^{-1}[H_{ref}(x, \omega)H_{sam}^*(x, \omega)], \quad (2.2)$$

where the axial depth z is the Fourier conjugate of ω , and $\mathcal{F}_{z\omega}^{-1}[\cdot]$ is the inverse Fourier transform about z . Before calculating Eq. (2.2), the measured power spectrum is rescaled with zero padding and linear interpolation, and the dispersion between the reference arm and sample arm is compensated numerically [49]. In the same manner, the vertical interference term $\tilde{I}_v(x, z)$ is extracted from the vertically polarized component of the interfered light $I_v(x, \omega)$.

When the fast axis of the EO modulator is oriented at $\pi/4$, the Jones matrix of the EO modulator can be expressed as

$$\begin{pmatrix} \cos \frac{\varphi}{2} & i \sin \frac{\varphi}{2} \\ i \sin \frac{\varphi}{2} & \cos \frac{\varphi}{2} \end{pmatrix}, \quad (2.3)$$

where φ is the phase retardation and modulated as $\varphi(x) = A_0 \sin(\omega_m x)$. ω_m is the driving frequency of the EO modulator, and x is the lateral position. As described in Sec. 2.2.3, discrete polarization modulation can also be used for the phase modulation of the EO modulator.

The Jones vector of the sample beam at the detector can be written as

$$\begin{pmatrix} H_{sam} \\ V_{sam} \end{pmatrix} = J_{all} \begin{pmatrix} H_i \\ V_i \end{pmatrix}, \quad (2.4)$$

where J_{all} is the overall round-trip Jones matrix including the birefringence of both the fiber and sample,

$$J_{all} = \begin{pmatrix} J(1,1) & J(1,2) \\ J(2,1) & J(2,2) \end{pmatrix}, \quad (2.5)$$

and $(H_i, V_i)^T$ is the Jones vector just after the EO modulator before the fiber coupler. When the incident beam to the EO modulator is vertically polarized,

$$\begin{pmatrix} H_i \\ V_i \end{pmatrix} = \begin{pmatrix} i \sin \frac{\varphi}{2} \\ \cos \frac{\varphi}{2} \end{pmatrix}. \quad (2.6)$$

The Jones vector $(H_{sam}, V_{sam})^T$ can be expressed as

$$\begin{pmatrix} H_{sam} \\ V_{sam} \end{pmatrix} = \begin{pmatrix} J(1,2) \cos \frac{\varphi}{2} + iJ(1,1) \sin \frac{\varphi}{2} \\ J(2,2) \cos \frac{\varphi}{2} + iJ(2,1) \sin \frac{\varphi}{2} \end{pmatrix}. \quad (2.7)$$

The Jones vector of the reference beam at the spectrometer is calibrated to be

$$E_{ref} = \begin{pmatrix} H_{ref} \\ V_{ref} \end{pmatrix} = \begin{pmatrix} H_r \\ V_r \end{pmatrix} e^{-i\frac{\varphi}{2}}, \quad (2.8)$$

where H_r and V_r are constants independent of the state of the EO modulator. The reference beam intensity at the CCD cameras should be flat and independent of the phase retardation of the EO modulator.

In our algorithm, Eq. (2.2) is Fourier transformed along x as

$$\mathcal{F}_{xu}[\tilde{I}_h(x)] = \mathcal{F}_{xu}[\mathcal{F}_{z\omega}^{-1}[H_{ref}(x, \omega)H_{sam}^*(x, \omega)]] \quad (2.9)$$

where $\mathcal{F}_{xu}[\cdot]$ is Fourier transform operator along x , and u is the Fourier conjugate of x . Equation (2.9) can be rearranged as

$$\begin{aligned} \mathcal{F}_{xu}[\tilde{I}_h(x)] &= H_r \mathcal{F}_{xu}[\mathbf{J}^*(1,2) \cos \frac{\varphi}{2} e^{-i\frac{\varphi}{2}} - i\mathbf{J}^*(1,1) \sin \frac{\varphi}{2} e^{-i\frac{\varphi}{2}}] \\ &= \frac{H_r}{2} \{ \mathcal{F}_{xu}[\mathbf{J}^*(1,2) - \mathbf{J}^*(1,1)] + \mathcal{F}_{xu}[\mathbf{J}^*(1,2) + \mathbf{J}^*(1,1)] * \mathcal{F}_{xu}[e^{-i\varphi}] \}, \quad (2.10) \end{aligned}$$

where $*$ denotes a convolution operator. Here, we omitted the argument z of these functions for simplicity. $e^{i\varphi}$ can be decomposed using the following relations:

$$\sin[\varphi(x)] = \sum_{l=0}^{\infty} 2J_{2l+1}(A_0) \sin[(2l+1)\omega_m x], \quad (2.11)$$

$$\cos[\varphi(x)] = J_0(A_0) + \sum_{l=1}^{\infty} 2J_{2l}(A_0) \cos[(2l)\omega_m x], \quad (2.12)$$

where the italic letters of J_0 , J_{2l} , and J_{2l+1} are the Bessel functions of the first kind of the order of 0, $2l$, and $2l+1$, respectively. We set the amplitude of the modulation to be $A_0 = 2.405$ radians to make $J_0(2.405) = 0$. Consequently, $\mathcal{F}_{xu}[e^{-i\varphi}]$ in Eq. (2.10) is rearranged to

$$\begin{aligned} \mathcal{F}_{xu}[e^{-i\varphi}] = & \sum_{l=0}^{\infty} \left[J_{2l}(2.405) \{ \delta(u - 2l\omega_m) + \delta(u + 2l\omega_m) \} \right. \\ & \left. + J_{2l+1}(2.405) \{ \delta(u - (2l+1)\omega_m) - \delta(u + (2l+1)\omega_m) \} \right]. \end{aligned} \quad (2.13)$$

The 1st and the 2nd terms of Eq. (2.10) are extracted by numerically clipping the 0th and 1st harmonic components of $\mathcal{F}_x[I_h(x)]$, respectively,

$$\tilde{I}_h(0) = \frac{H_r}{2} (J^*(1, 2) - J^*(1, 1)), \quad (2.14)$$

$$\tilde{I}_h(\omega_m) = \frac{J_1(2.405)H_r}{2} (J^*(1, 2) + J^*(1, 1)), \quad (2.15)$$

because these terms are distinct from each other in frequency. $J(1, 1)$ and $J(1, 2)$ are calculated as

$$H_r J^*(1, 1) = - \left\{ \tilde{I}_h(0) - \frac{1}{J_1(2.405)} \tilde{I}_h(\omega_m) \right\}, \quad (2.16)$$

$$H_r J^*(1, 2) = \left\{ \tilde{I}_h(0) + \frac{1}{J_1(2.405)} \tilde{I}_h(\omega_m) \right\}. \quad (2.17)$$

In the same manner, $V_r J^*(2, 1)$ and $V_r J^*(2, 2)$ are calculated from the vertically polarized component of the spectrum, $I_v(x, \omega)$. H_r and V_r can be omitted because $|H_r|$ and $|V_r|$ are identical, and $\gamma \equiv \arg(H_r) - \arg(V_r)$ is included in the fiber-induced birefringence described in Sec. 2.2.2. As a result, we obtain the following matrix,

$$\begin{pmatrix} H_r^* J(1, 1) & H_r^* J(1, 2) \\ V_r^* J(1, 1) & V_r^* J(1, 2) \end{pmatrix} = \begin{pmatrix} 1 & 0 \\ 0 & e^{i\gamma} \end{pmatrix} J_{all} = J_{offset} J_{all}, \quad (2.18)$$

where we term the offset caused by H_r and V_r as J_{offset} .

2.2.2 Compensation of the fiber-induced birefringence

To obtain the Jones matrix of the sample, fiber-induced birefringence should be canceled from J_{all} . This can be achieved by using the algorithm developed by Park et al. [39, 50]. We assume the surface of the sample to be a mirror. Note that even if the surface tissue has birefringence, this algorithm is valid as long as the backscattering does not change the polarization. The Jones matrix at the surface of the sample can be expressed as

$$J_{sur} = J_{out}J_{in}, \quad (2.19)$$

where J_{in} and J_{out} are Jones matrices corresponding to the fiber components between the EO modulator and sample surface and that of the sample surface and polarizing beamsplitter in the spectrometer, respectively. J_{all} includes the round-trip Jones matrix of the sample J_{sam} , i. e.,

$$J_{all} = J_{out}J_{sam}J_{in}. \quad (2.20)$$

We can measure only $J_{offset}J_{sur}$ and depth-resolved $J_{offset}J_{all}$. In order to obtain J_{sam} , J_{in} is eliminated by multiplying $J_{offset}J_{all}$ by $(J_{offset}J_{sur})^{-1}$ and diagonalization is performed as

$$\begin{aligned} J_{offset}J_{all}(J_{offset}J_{sur})^{-1} &= J_{offset}J_{out}J_{sam}J_{in}J_{in}^{-1}J_{out}^{-1}J_{offset}^{-1} \\ &= J_{offset}J_{out}J_{sam}J_{out}^{-1}J_{offset}^{-1} \\ &= J_U \begin{pmatrix} p_1 e^{i\frac{\eta}{2}} & 0 \\ 0 & p_2 e^{-i\frac{\eta}{2}} \end{pmatrix} J_U^{-1}, \end{aligned} \quad (2.21)$$

where p_1 and p_2 are the attenuation coefficients of the sample; η , the retardation of the sample; and J_U , an unitary matrix. We can calculate the relative optic axis, retardation, and diattenuation of the sample from this diagonalization [39]. Since the Jones matrix is directly obtained in our algorithm described in Sec. 2.2.1, we calculated the matrix diagonalization directly.

2.2.3 Discrete polarization modulation

Since the incident polarization is modulated along the B-scan, it is preferable to reduce the sampling data sets to calculate the spatial frequency. When the number of sampling data sets is reduced in our algorithm, it causes fringe washout because the incident polarization is modulated during the A-scan. From Eq. (2.10), we can see that the fringe washout affects the 1st order of the spatial frequency but does not affect the 0th order of the spatial frequency. Since the fringe washout occurs for the power spectrum originally measured (and not the spatial frequency), it causes both the SNR penalty of the intensity and the polarimetric artifact. Although it is difficult to quantitatively evaluate them in a biological sample because the measured intensity is not always the same even if we measure the same area, we can avoid the fringe washout using the equivalent discrete polarization modulation instead of the continuous polarization modulation.

When N A-scans are measured for a cycle of incident polarization modulation, the average phase retardation of the EO modulator φ_n at the n th A-scan is

$$\varphi_n = \frac{\int_{2\pi(n-1)/N}^{2\pi n/N} A_0 \sin(\omega_m x) dx}{2\pi/N}, \quad (2.22)$$

where $n = 1, 2, \dots, N$. When $N = 3$, the set discrete phase retardation $\varphi_1, \varphi_2, \varphi_3$ are $\frac{9}{4\pi}A_0, 0, -\frac{9}{4\pi}A_0$, respectively. As shown later in Sec. 2.3.1 and Fig. 2.5(a)-(c), the fringe washout caused by continuous polarization modulation is not critical. However, this discrete polarization modulation is equivalent to the continuous polarization modulation, and avoids fringe washout.

In our method, at least three incident polarization states are required. Compared with the method previously developed by Park et al. using two incident polarization states [43], our method requires larger overall amount of data. Although it is expected that three or more incident polarization states decrease the SNR, currently it is not clear, and further theoretical and experimental analysis is needed.

2.3 Experimental results and discussion

2.3.1 Measurements of a polarizer and a waveplate

To validate our method, a linear polarizer (LP) and a quarter waveplate (QWP) are investigated. For both LP and QWP, the front surface was used for J_{sur} and the back surface was used for J_{all} . The EO modulator was continuously modulated at 4 A-scans/cycle during 512 A-scans. J_{all} was calculated and averaged for 512 A-scans. LP and QWP are rotated from 0 to 180 deg. The measured cumulative relative orientation of LP and QWP and the round-trip phase retardation of QWP are shown in Fig. 2.3. The diattenuation of LP was 0.999 ± 0.001 . These results agreed with the theoretical expectation. The round-trip phase retardation of QWP was 170 ± 3 degrees. Since the phase retardation exceeding 180 degrees is phase-wrapped, the phase retardation of QWP is smaller than 180 degrees [51].

2.3.2 Measurements of biological samples

Figure 2.4 shows the intensity and phase retardation images of chicken breast muscle, where glycerin was applied on the sample surface. Instead of the continuous polarization modulation, equivalent discrete polarization modulation was used for the biological measurements, as shown in Figs. 2.4, 2.5(d)-(e), 2.6, and 2.7, except Fig. 2.5(a)-(c). For all measurements of the biological samples, the incident polarization is modulated as a 3 A-lines/cycle, and the lateral measurement area for one cycle is well below the transversal resolution. For three dimensional measurement, the data acquired by the framegrabber from the cameras are immediately transferred to the main memory on the motherboard (S2895, Tyan, CA, USA). The maximum number of measurement points is limited by the memory space per process of 32 bit Windows XP,

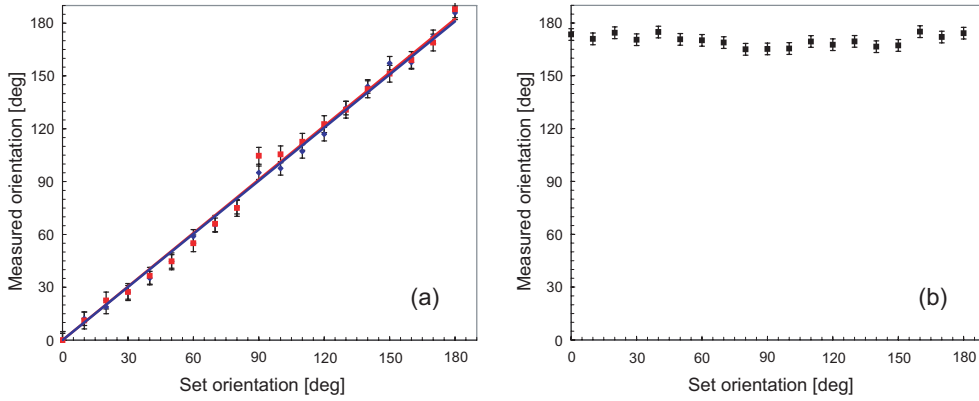


Figure 2.3: (a): measured orientations of LP and QWP. The rhombuses and squares are the measured cumulative orientation of LP and QWP relative to 0 degree, respectively. The solid and dashed lines are the linear least-squares fits of the orientations of LP and QWP, respectively. (b): measured phase retardation of QWP.

namely, 2 GB. In order to remove the fixed pattern noise mainly from the EO modulator, the OCT signal is first divided to each state of the incident polarization before calculating the Jones matrix. The fixed pattern noise is removed from the aligned images by low-pass filtering of the averaged spectrum [52], because the phase of the fixed pattern noise for each incident polarization is different. After the removal, the image is realigned with the initial order, and the Jones matrix is calculated. One pixel is extracted as the surface of the sample for each A-scan, and the Jones matrices at these pixels are averaged for 3D volume to determine J_{sur} . Figure 2.4(a) is an intensity image generated by

$$10 \log \left\{ \frac{1}{2} (|J(1, 1)|^2 + |J(1, 2)|^2 + |J(2, 1)|^2 + |J(2, 2)|^2) \right\}, \quad (2.23)$$

which corresponds to the element of the 1st row and 1st column of the Mueller matrix, m_{00} . Figure 2.4(b) is a cumulative round-trip phase retardation image. The phase retardation image is gray-scaled to represent it from 0 to π . Because of the form birefringence and cumulative nature of the measured J_{sam} , Fig. 2.4 (b) shows periodic changes in the phase retardation. Although the phase retardation is not uniform, the three dimensional image shows that the nonuniformity is not an artifact but a certain structure. The orientation image in Fig. 2.4(c) were generated by using half the absolute angular difference between the eigenpolarizations of the surface and a certain depth on the Poincaré sphere. In this simplified case, the range of the orientation is 0 to $\pi/2$. We can see the periodic abrupt changes due to the phase unwrapping in Figure 2.4 (c) [53].

Figure 2.5 shows intensity, phase retardation, and orientation images of chicken breast muscle to compare continuous polarization modulation (Fig. 2.5(a)-(c)) and discrete polarization modulation (Fig. 2.5(d)-(f)). For both measurements, the incident polarization was modulated as

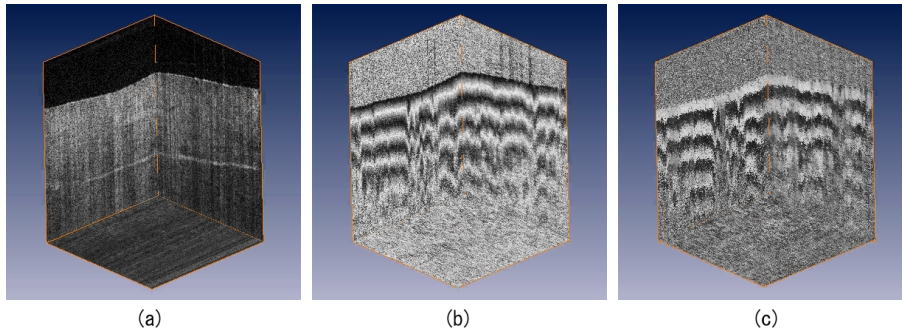


Figure 2.4: An intensity image (a), the cumulative round-trip phase retardation image (b), and the orientation image (c) of chicken breast muscle. A median filter with a kernel size of 3×3 was applied to each B-scan of (b) and (c). Each frame has 1023 A-lines, and 128 frames are acquired in 5 seconds. The image size is 2 mm (x) \times 2 mm (y) \times 3.44 mm (z) in air.

a 3 A-lines/cycle, and same area on the sample was scanned. In this measurement, the difference of the polarization modulation was appeared in the orientation images (Fig. 2.5(c) and (f)). Fig. 2.5(c) had smaller axial changes due to the phase unwrapping. As predicted in Sec. 2.2.3, discrete polarization modulation is better choice for our B-scan-oriented polarization modulation method.

Figure 2.6 shows the intensity and phase retardation images of a human finger pad *in vivo*. According to the previous reports, the cumulative phase retardation of the dermis has a lateral structure, while the birefringence of the stratum corneum has a random nature [43,54,55]. Sweat ducts in the stratum corneum have low birefringence. A movie showing the orthoslices reveal that the phase retardation of the dermis corresponds to the pattern of the follicles, as given in the previous reports [43, 54, 55].

Figure 2.7 shows a caries lesion of a human canine tooth *in vivo*. The tooth was horizontally scanned for each frame. The arrow in the intensity image of Fig. 2.7(a) shows the enamel-dentin junction. In the enamel region, the incremental lines, which are result of irregularities in enamel formation, can be found. The tufts and lamellae were observed above the enamel-dentin junction in the intensity image. Birefringence was observed in the enamel layer, which corresponds to the enamel prisms [29]. In the deeper area including the dentin, the pattern of the cumulative phase retardation changes frame by frame. In the caries region strong scattering was observed and the birefringence was random. This probably corresponds to demineralization in the enamel resulting in caries formation [29].

In this paper, we used the range of the phase retardation from 0 deg to 180 deg, which is direct result of Eq. (2.21). The other way to represent the phase retardation is unfolding it from 0 deg to 360 deg by shortening the range of the orientation [53]. For fully fiber-based system, determination of the rotating plane of the orientation in a Poincaré sphere is required in order to

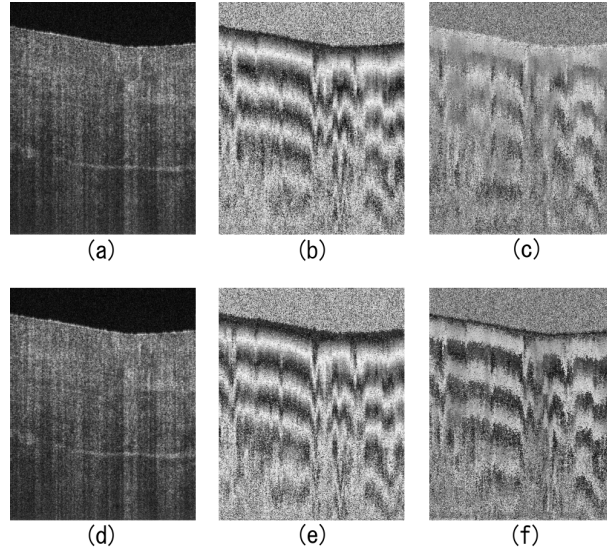


Figure 2.5: Images of chicken breast muscle with different modulations. Upper images (a)-(c) are measured with continuous polarization modulation, and lower images (d)-(f) are measured with discrete polarization modulation. (a) and (d) are the intensity images, (b) and (e) are the phase retardation images, and (c) and (f) are the orientation images. All images have 1023 A-lines, and axial 500 pixels. The image size is 2 mm (x) \times 2.15 mm (z) in air.

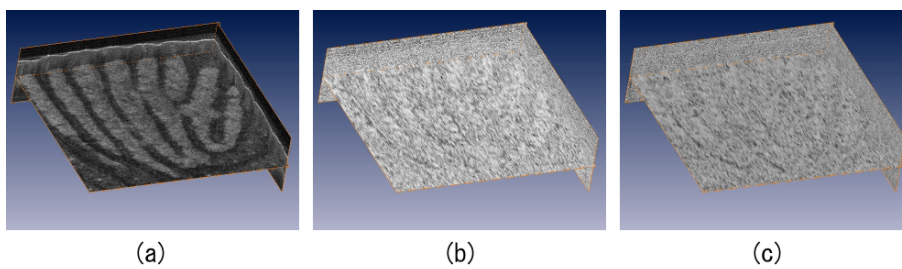


Figure 2.6: An intensity image (a), the cumulative round-trip phase retardation image (b), and the orientation image (c) of a human finger pad *in vivo*. A median filter with a kernel size of 3×3 was applied to each B-scan of (b) and (c). The volume is 4 mm (x) \times 4 mm (y) \times 1.75 mm (z) in air, or 1023 pixels \times 128 pixels \times 350 pixels. The measurement time is 5 seconds.

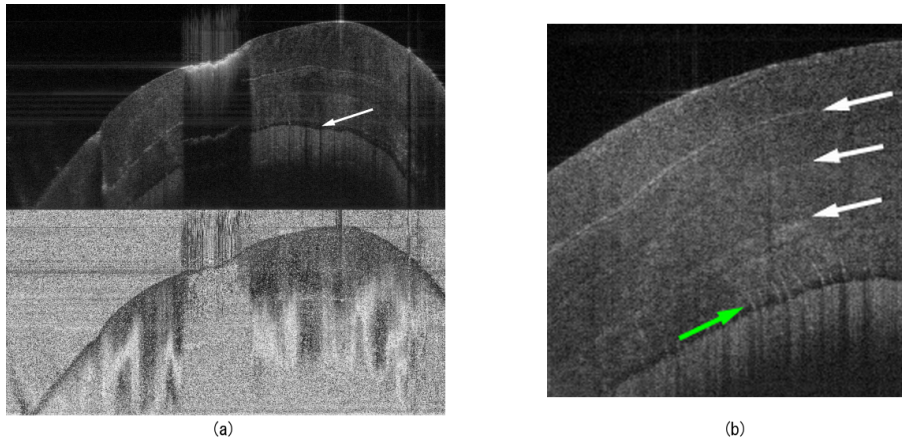


Figure 2.7: (a): an intensity image (upper) and the cumulative round-trip phase retardation image (lower) of caries lesion of human canine tooth *in vivo*. A white arrow shows the enamel-dentin junction. The size is 6 mm (x) \times 2.80 mm (z) in air, or 2046 pixels (x) \times 650 pixels (z). 64 frames were scanned on 6 mm length and acquired in 5 s. (b): a enlarged intensity image of the 24th frame in the movie (a). The white arrows show the incremental lines in the enamel region. A green arrow shows the tufts and lamellae above the enamel-dentin junction. The image size is 2.5 mm (x) \times 2.54 mm (z) in air.

obtain the orientation from -90 deg to $+90$ deg [43]. Since the orientation of biological samples is often noisy, we used the direct result of the phase retardation ranging from 0 deg to 180 deg. In this case, however, all noise of the phase retardation near 180 deg decreases the measured phase retardation, as indicated in Sec. 2.3.1. For example, the phase retardation of 190 deg becomes 170 deg. This problem can be solved by unfolding the phase retardation, with stable way to determine the rotating plane of the orientation for biological samples [43].

2.4 Summary

In conclusion, we developed the PS-FD-OCT system at 840 nm using polarization modulation method along B-scan. The incident polarization was modulated along a lateral B-scan on the sample. Instead of continuous polarization modulation along B-scan, equivalent discrete polarization modulation was used in order to avoid the fringe washout. By extracting the 0th and 1st order of the spatial frequencies along the B-scan of the FD-OCT, the two-dimensional Jones matrix of the sample was measured. The detailed calibration procedure of the spectrometer was shown. Fiber-induced birefringence was compensated by matrix diagonalization. The proposed algorithm and system was confirmed with LP and QWP measurements. Using the PS-FD-OCT system, the phase retardation of chicken breast muscle, a finger pad, and a caries lesion of a tooth

was successfully imaged.

Chapter 3

Application of PS-SD-OCT for the phase retardation measurement of retinal nerve fiber layer

Abstract

Phase retardation of *in vivo* human retinal nerve fiber layer (RNFL) is quantitatively measured by two methods— polarization-sensitive spectral-domain optical coherence tomography (PS-SD-OCT) and scanning laser polarimetry (SLP). An *en face* cumulative phase retardation map is calculated from the three-dimensional phase retardation volume of healthy and glaucomatous eyes measured by PS-SD-OCT. It is shown that the phase retardation curves around the optic nerve head measured by PS-SD-OCT and SLP have similar values except near the retinal blood vessels. PS-SD-OCT can measure the cumulative phase retardation of RNFL as well as SLP, which will allow the evaluation of RNFL for glaucomatous eyes.

3.1 Introduction

Glaucoma is an optic neuropathy that causes the loss of retinal ganglion cells and damage to the retinal nerve fiber layer (RNFL). It causes progressive and irreversible vision loss if left untreated. The early detection of glaucoma is important because it progresses even before visual field loss can occur [56]. Visual field test and ophthalmoscopic assessment of a optic nerve head are subjective methods to diagnose glaucoma. Since the thinning of RNFL is a direct indicator of glaucoma, glaucoma can also be diagnosed by objective measurement of RNFL thickness. Objective and quantitative measurements of RNFL have certain advantages over the subjective methods because in these methods, the intervention of experts becomes unnecessary and statistical diagnostic analysis is possible. Therefore, methods such as OCT and scanning laser polarimetry (SLP) have been utilized.

OCT can measure the depth-resolved backscattering intensity image of the sample. Schuman et al. first measured the thickness of RNFL by OCT [57]. Thickness measurement using OCT images has certain limitations, namely, the requirement of high axial resolution and a high-quality algorithm for boundary segmentation.

GDx-VCC (Carl Zeiss Meditec) is a commercially available SLP, that provides an RNFL thickness map by converting the phase retardation of RNFL, assuming that the birefringence of RNFL is constant [58,59]. It compensates for the corneal birefringence by monitoring a bow-tie pattern in the macular region and measures the combined effect of the thickness and birefringence of RNFL and diagnoses glaucoma statistically using the normative database [60].

PS-OCT has been developed to measure the depth-resolved birefringence of biological samples [10, 11]. By using PS-OCT, *in vivo* human retina was first examined by Cense et al. [61]. Pircher et al. showed polarization scrambling at retinal pigment epithelium in the macular region [62]. The recent development of spectral-domain OCT (SD-OCT) revealed that SD-OCT had a higher signal-to-noise ratio than the conventional time-domain OCT [2,3]. By using high-speed and highly sensitive SD-OCT, it is possible to measure three-dimensional retina *in vivo* [6]. High-speed retinal SD-OCT was adapted to PS-OCT by Cense et al. [44]. Göttinger et al. demonstrated three-dimensional phase retardation images and optic axis images of the retina by using the free-space PS-SD-OCT system [16]. One characteristic of PS-OCT is that corneal birefringence compensation is possible by using the surface signal [37,39,40]. In retinal imaging, the signal from the anterior boundary of the retina can be used as the surface signal. Unlike SLP, this corneal compensation does not rely on healthy macula. The other characteristic is the ability to measure the thickness and birefringence of RNFL simultaneously. Cense et al. showed that the birefringence of RNFL has angular dependence around the optic nerve head [14,63]. Mujat et al. showed an *en face* birefringence map of RNFL for the first time [64]. In contrast, SLP measures the *en face* phase retardation map, that is, the combined effect of the thickness and birefringence of RNFL. Although by using PS-OCT it is possible to measure thickness and birefringence separately, birefringence measurement is less reliable in the case of a thin RNFL [14,44]. In addition, the diagnostic performance of PS-OCT with regard to glaucoma has not yet been demonstrated.

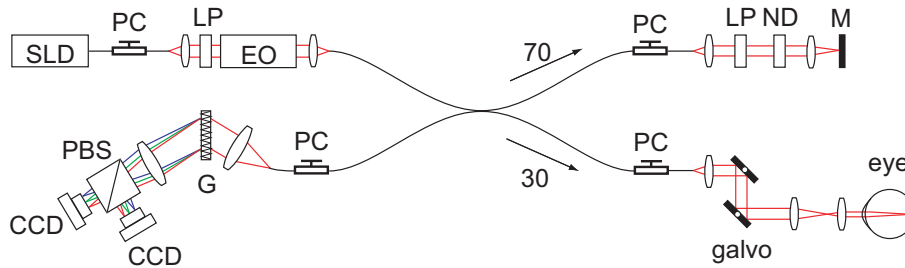


Figure 3.1: Diagram of the PS-SD-OCT system for the retinal imaging. The following notations are used: SLD: superluminescent diode, PC: polarization controller, ND: neutral density filter, LP: linear polarizer, EO: electro-optic modulator, M: mirror, G: grating, PBS: polarizing beamsplitter, CCD: line-CCD camera.

Since it is known that SLP gives a good performance in the diagnosis of glaucoma [65–67], a comparison of PS-OCT and SLP is of significant interest in the preliminary research on the detection of glaucoma using PS-OCT. Previously, Huang et al. measured birefringence of RNFL by using thickness measured by conventional OCT and phase retardation measured by SLP [68]. Wojtkowski et al. compared thickness map of RNFL measured by SD-OCT and phase retardation map measured by SLP [69]. However, there is still no report about the comparison between PS-OCT and SLP. In this chapter, we describe a pilot study on the quantitative comparison of the phase retardation of RNFL using PS-OCT and SLP for both healthy and glaucomatous eyes.

3.2 Methods

3.2.1 PS-SD-OCT system

The details of the PS-SD-OCT system employed in this study have been described in Chapter 2 and the reference [45]. In brief, the schematic diagram of our system is shown in Fig. 3.1. In the sample arm, an imaging plane made by the objective lens ($f = 50$ mm) is relayed by a Volk ophthalmic lens (78D) to the retina. The probing power is $700 \mu\text{W}$. The other parts of the optical components and the method to obtain the intensity, diattenuation, phase retardation, and relative orientation are described in Chapter 2.

3.2.2 Three-dimensional volumetric measurement by PS-SD-OCT

Since the RNFL in the peripheral region contains nerve fibers that are all diverging from the optic nerve head, SLP diagnoses glaucoma by measuring the *en face* phase retardation of RNFL in the peripheral region. By using our PS-SD-OCT system, the three-dimensional intensity and phase retardation volumes in the peripheral region are measured. The measurement range is 3.76

mm \times 3.76 mm on the retina. The probe beam is scanned from the nasal to the temporal regions with 1023 A-lines for each B-scan. The lateral density of the A-lines is 3.7 $\mu\text{m}/\text{A-line}$, which is well below the lateral spot size of our system, that is, 27 μm . This setup is attributed to the high dense scan required for PS-OCT with multiple incident polarizations [43]. The raster scanning from inferior to superior is performed with 140 B-scans in 5.5 s. This protocol is used for all PS-SD-OCT measurements described in this chapter.

3.2.3 *En face* phase retardation maps

To compare the *en face* phase retardation maps of SLP and PS-SD-OCT, the three-dimensional phase retardation volume measured by PS-SD-OCT was shrunk into the *en face* map using the following comparable method. The main contribution to the SLP signal is high scattering from the layers beneath the RNFL, such as the interface of the inner and outer segments of the photoreceptor layers (IPRL) and the retinal pigment epithelium (RPE). Thus, it is reasonable to extract the backscattered signal from these high scattering layers in the PS-SD-OCT images in order to compare these two systems. The cumulative phase retardation of PS-OCT from the lower layers corresponds to the double-pass phase retardation of the RNFL because there is no birefringent tissue between the posterior boundary of RNFL and RPE [15, 16]. It is known that RPE has polarization scrambling in macula [16, 62]. The detail of polarization scrambling in the peripheral region has not been studied yet. In our experiment, polarization scrambling was not observed at the RPE on the periphery of the optic nerve head as shown in Fig. 3.2 (c). Since RPE has the strongest signal in the retinal image, the segmentation of RPE layer is stable and easy. Hence, in this paper, we extract the signal from the RPE in the PS-SD-OCT images to make an *en face* phase retardation map. However, some studies have reported polarization scrambling in the peripheral region [16, 55], and it is not always guaranteed that our method is applicable. Other highly backscattering layers, e.g. IPRL, would be the candidates to avoid the possible polarization scrambling for the future version of this method.

A large white and yellow spot in Figs. 3.2 (b) and (c) (indicated by arrows) are phase retardation artifacts caused by Doppler signal of the blood flow. In our algorithm of PS-SD-OCT, we cannot discriminate the phase change caused by Doppler flow from real birefringence. However, this artifact is localized in a blood vessel and does not affect the phase retardation of RPE.

In order to extract the phase retardation at the RPE, first the RPE layer is segmented from the intensity images. For this purpose, the maximum gradient points are detected below the anterior boundary of the retina and smoothed to interpolate the shadow of blood vessels for each B-scan intensity image [70]. Figure 3.2 (d) shows the segmented RPE, it indicates our segmentation algorithm works well. Even if the detected layer is slightly deviated, for example, an IPRL was faulty selected, the phase retardation does not change drastically (Fig. 3.2 (b)). This is because the alternation of the phase retardation occurs in RNFL and the small fluctuation of the segmentation does not affect to the detected phase retardation value. No smoothing algorithm was employed for the phase retardation images. The same procedure is applied to all B-scan

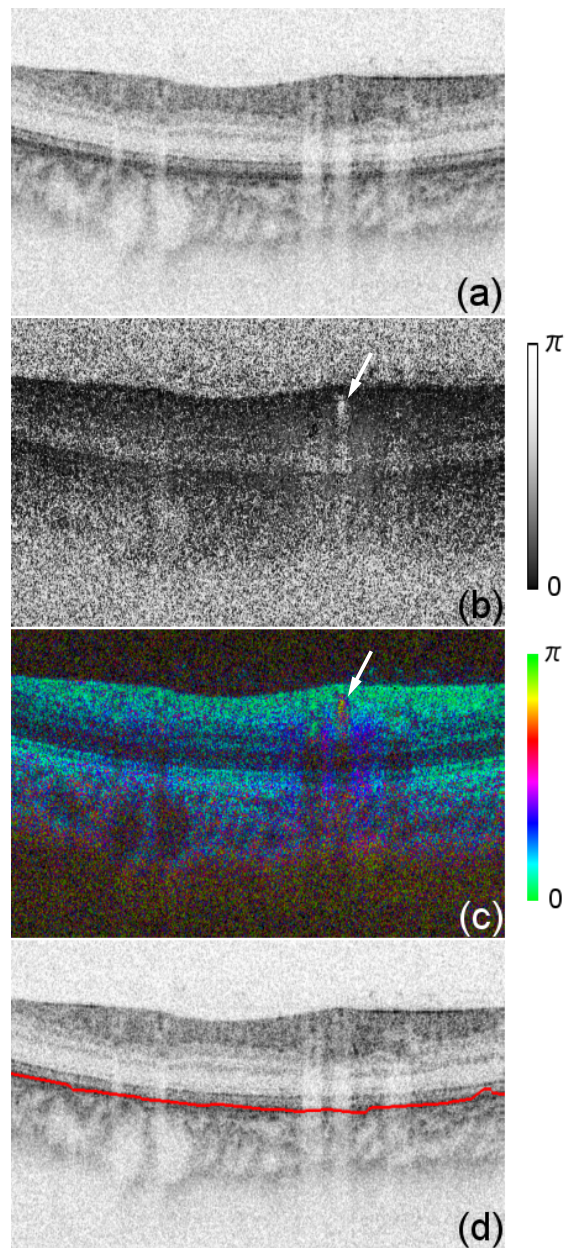


Figure 3.2: Intensity image (a), double-pass cumulative phase retardation image (b), and composite image (c) of inferior of an optic nerve head of a healthy human left eye. The image size is $3.76 \text{ mm} \times 0.94 \text{ mm}$. The longitudinal scale is enlarged to twice the lateral scale. The range of the phase retardation is from 0 to π radians (0 to 180 degrees) in double pass. White arrows in (b) and (c) indicate an artificial phase retardation in the blood vessel. A red line over the intensity image in (d) indicates the segmented RPE layer.

stacks, and an *en face* phase retardation map at the RPE position is obtained.

3.2.4 Quantitative analysis of phase retardation

For the quantitative comparison of PS-SD-OCT and SLP, the cumulative phase retardation of RNFL in the peripheral region is examined because nerve fibers diverge from the optic nerve head. For this purpose, the phase retardation around the optic nerve head is extracted from the *en face* phase retardation map.

GDx-VCC has a function that shows the RNFL thickness curve in the annular area of the *en face* phase retardation map. The RNFL thickness curve measured by GDx-VCC was converted into the double-pass phase retardation by using a conversion factor of $0.62 \text{ deg}/\mu\text{m}$ [71].

An annular area with an outer radius of 1.6 mm and an inner radius of 1.2 mm was set in order to extract the phase retardation of PS-SD-OCT; this setting is identical to that used in GDx-VCC. We evaluated two methods for calculating the phase retardation curve of PS-SD-OCT. In the first simple method, the phase retardation of PS-SD-OCT in the annular area was calculated using simple moving average with the kernel size of 9° . Second, the following histogram-based method is also evaluated as an alternative to the first method. Histograms of small angular areas (9°) within the ring are obtained and the mode value of the histogram is calculated. The small angular area is moved along the circumference, and the mode values are calculated for each small angular area. After moving average with a kernel of 3.6° , the phase retardation curve is obtained.

3.3 Results and discussion

3.3.1 Subjects

All experiments were performed using a protocol that adheres to the tenets of Declaration of Helsinki and was approved by the Institutional Review Board of University of Tsukuba and Tokyo Medical University. As the healthy subject, a volunteer (25-year-old Japanese male) without any detectable ocular disease was selected. As the glaucoma subject, a volunteer (42-year-old Japanese male) with glaucoma was selected. For both volunteers, the left eyes were examined.

3.3.2 Three-dimensional phase retardation volume

Figure 3.3 shows the three-dimensional intensity and phase retardation image measured by PS-SD-OCT in the retinal peripheral region of the retina. The figure on the left in Fig. 2 shows the phase retardation volume with a front view from the anterior side, while the one on the right shows the rear view from the posterior side. The hue of its colormap corresponds to the phase retardation from 0° to 180° , while the opacity corresponds to the intensity.

Several structures were observed in the three-dimensional phase retardation map similar to the previous report [16]. In the front view of Fig. 3.3, the phase retardation was nearly 0 because fiber-optic and corneal birefringence, which causes phase retardation artifacts in the retina, was

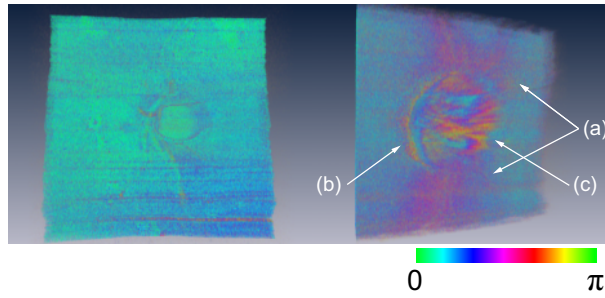


Figure 3.3: Front view (left) and rear view (right) of the three-dimensional phase retardation image of a healthy eye in the peripheral region. A measurement range of $3.76 \text{ mm} \times 3.76 \text{ mm}$ ($13.1 \text{ deg} \times 13.1 \text{ deg}$) was scanned on the sample. The hue of the color bar is same as that in Fig. 3.2.

compensated using a reference signal of the retinal surface [72, 73]. In the inferior and superior regions, the high phase retardation beneath the surface was visible because the volume image was semi-transparent. In the rear view, the double-hump pattern of the phase retardation was observed in the superior and inferior regions of the optic nerve head (a). The phase retardation also changed at the temporal edge of the optic nerve head (scleral canal rim) (b) and the lamina cribrosa in the optic nerve head (c).

Figure 3.4 shows the *en face* phase retardation maps on the surface of retina. For the better visualization, high threshold was set in order to segment the first intensity peak on the surface rather than the boundary between the noise and signal areas. The phase retardation map of the glaucomatous eye had higher speckle noise than that of the healthy eye. In both maps, the phase retardation had high values at the edge of the optic disc because of an error of the surface segmentation. Since there was no radial variation of the phase retardation, residual effect of the fiber-optic and corneal birefringence could be negligible. Figure 3.5 shows the histogram of the phase retardation on the surface of retina. The mode values of the healthy and glaucomatous eyes were 17.0 deg and 18.8 deg , respectively. Since all noise near zero retardation affects the result to a positive direction, the histogram had asymmetric distribution and the phase retardation diverged from zero.

Figure 3.2 shows the intensity (a) and phase retardation (b) images of a healthy human retina at the superior uppermost B-scan in Fig. 3.3. The retinal layers are clearly visible in the intensity image similar to the previous report [14]. In the thick RNFL area, the phase retardation evidently changes. It has a noisy appearance in low-intensity area such as the outer nuclear layer and shadow beneath the retinal blood vessels. Figure 3.2 (c) is the composite image of the intensity and phase retardation images. In the composite image, the hue corresponds to the phase retardation, while the brightness corresponds to the intensity. In the composite image, the phase retardation with high signal intensity is shown in a bright color. Hence, both intensity and

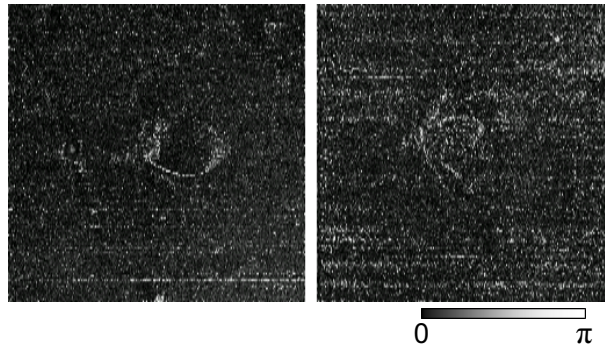


Figure 3.4: The phase retardation maps of the healthy eye (left) and glaucomatous eye (right) on the surface of retina.

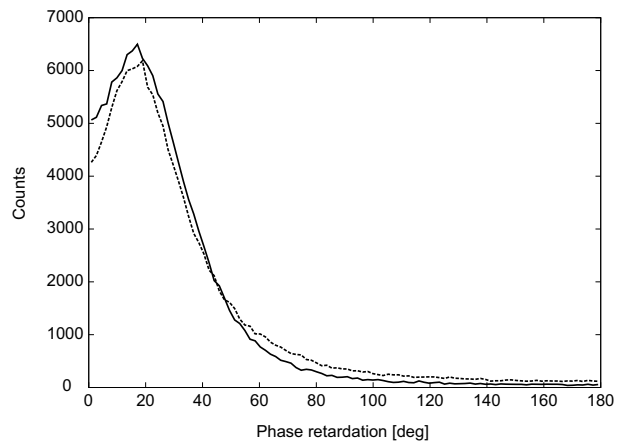


Figure 3.5: The histograms of the phase retardation of the healthy eye (solid line) and glaucomatous eye (dashed line) on the surface of retina.

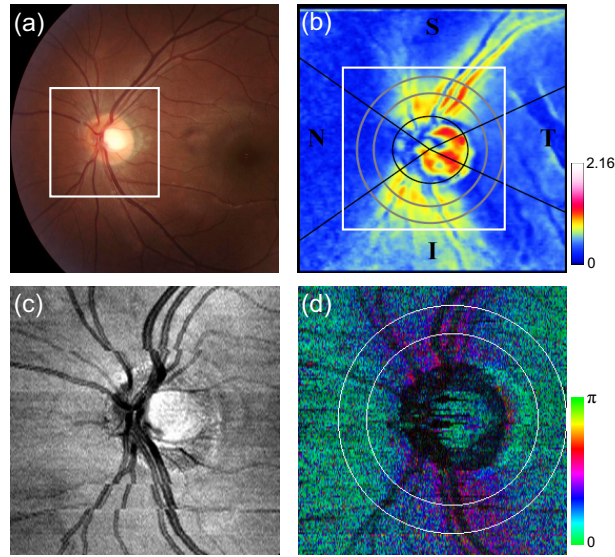


Figure 3.6: Fundus image (a), nerve fiber thickness map measured by GDx-VCC (b), *en face* projection image of the OCT intensity (c), and *en face* phase retardation image measured by the PS-SD-OCT (d) for the healthy eye. The fundus image was measured by a non-mydratric fundus camera. Measurement ranges of $5.8 \text{ mm} \times 5.8 \text{ mm}$ ($20 \text{ deg} \times 20 \text{ deg}$) and $3.76 \text{ mm} \times 3.76 \text{ mm}$ ($13.1 \text{ deg} \times 13.1 \text{ deg}$) were scanned on the sample for GDx-VCC and PS-SD-OCT, respectively. An annular area indicated by two white circles in the phase retardation image of PS-SD-OCT is used to calculate the graph of the phase retardation shown in Fig. 3.7.

phase retardation can be viewed in one image. This color map is also used for the *en face* phase retardation map in the following sections.

3.3.3 Healthy eye

Figure 3.6 shows the *en face* phase retardation maps of GDx-VCC (b) and PS-SD-OCT (d) of a healthy human volunteer. The annular areas for the quantitative analysis are indicated by gray and white circles in Figs. 3.6 (b) and (d), respectively. The fundus image (a) and OCT projection image (c) are also shown. The OCT projection image was calculated by summing each A-line of the linear OCT intensity signal. The *en face* phase retardation images of both GDx-VCC and PS-SD-OCT showed a similar double-hump pattern, which is consistent with the typical distribution of RNFL of healthy eyes.

Figure 3.7 shows the phase retardation curves of a healthy eye. The dotted line in Fig. 3.7 shows the phase retardation of PS-SD-OCT in the annular area calculated by the simple moving average. The curve takes extremely high values as compared to the curve of GDx-VCC. This is because the phase retardation ranges from 0 to π and has a strongly asymmetric distribution.

Therefore, averaging is not appropriate for this case.

The phase retardation curve calculated by the second histogram-based method is shown in Fig. 3.7 by a solid line. The high phase retardation in the temporal and nasal regions obtained in the first method was decreased in the second method, which is reasonable because of the non-Gaussian distribution of the phase retardation.

The curves of both PS-SD-OCT and GDx-VCC showed humps in the superior and inferior regions. In the case of PS-SD-OCT, the phase retardation inferior to the optic nerve head had the maximum value. Both the superior and inferior peaks of PS-SD-OCT were higher than that of GDx-VCC. Although its reason is not clear, the curve of GDx-VCC had a flatter shape in the inferior region. The uneven curve of PS-SD-OCT is a reasonable result of thick RNFL in the inferior region as shown in the intensity image.

To observe the correlation between the phase retardation and the retinal structure, the OCT intensity image at the center of the peripheral annular area is shown in the upper image of Fig. 3.7. The shadows beneath the retinal blood vessels are represented in the phase retardation graph as gray masks. The phase retardation had local peaks on one side or both sides of some blood vessels, as indicated by arrows in Fig. 3.7. The possible reason for this is that the phase retardation was affected by thick RNFL around the retinal blood vessels. In contrast, GDx-VCC did not show such sharp peaks in Fig. 3.7. However, we can see the peaks of the phase retardation in the *en face* phase retardation map measured by GDx-VCC in Fig. 3.6 (b). For example, there are three peaks in the temporal superior area of the calculation ring of Fig. 3.6 (b), but they are combined into a single peak in the curve of Fig. 3.7. This means that GDx-VCC also measures such peaks near blood vessels as PS-SD-OCT, but they are largely smoothed in the curve of Fig. 3.7. Therefore, the difference near blood vessels in Fig. 3.7 was caused by the difference between the calculation procedures of PS-SD-OCT and GDx-VCC.

In order to check the birefringence of RNFL, we manually segmented the thickness of RNFL using the intensity image of Fig. 3.7 and calculated the double pass phase retardation per unit depth (DPPR/UD). Figure 3.8 shows the thickness and DPPR/UD of the healthy eye. The DPPR/UD in superior and inferior regions are higher than the temporal and nasal regions. Both of the thickness and DPPR/UD are in the same order of that reported previously [14, 63].

3.3.4 Glaucomatous eye

A glaucoma patient was also examined using the same scheme. Figure 3.9 shows the visual field test of the glaucomatous eye with the full threshold method on the central 24 degrees of the visual field. The glaucomatous eye has severe loss of inferior visual field and moderate loss of superior visual field.

Figure 3.10 shows the *en face* phase retardation map of the glaucomatous eye measured by PS-SD-OCT and GDx-VCC. The lateral quick motion in the inferior region was manually compensated. The double-hump patterns of the glaucomatous eye obtained from both PS-SD-OCT and GDx-VCC were degraded as compared to that of the healthy eye shown in Fig. 3.6 (b)

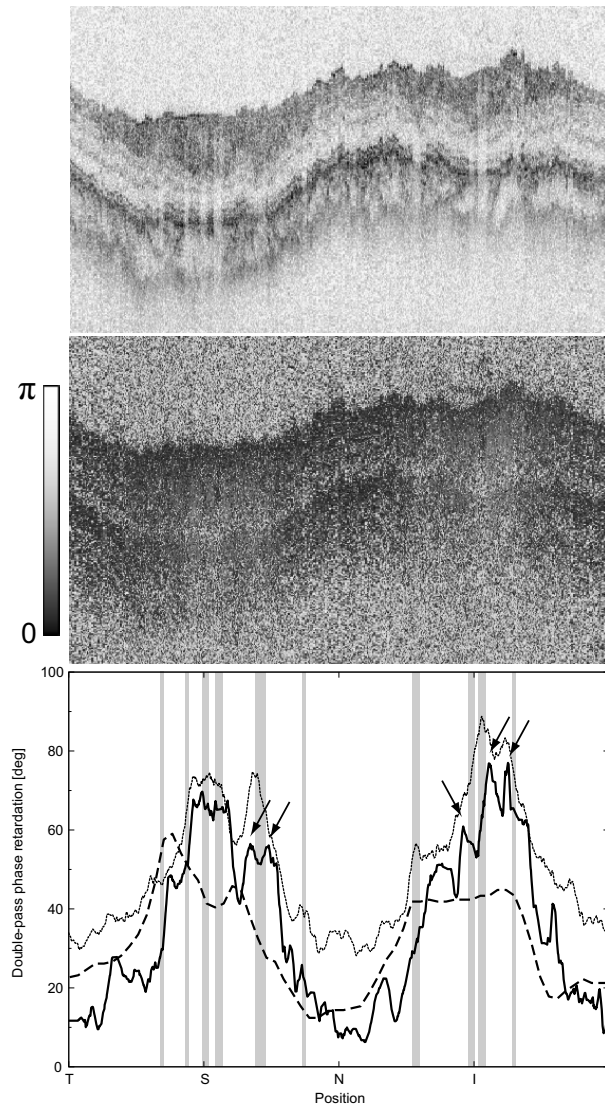


Figure 3.7: The upper image shows the OCT intensity at the center of the peripheral annular area of the healthy eye. The middle image shows the phase retardation image at the same position of the upper intensity image. The axial range of these images is 0.96 mm. The lower figure shows the round-trip cumulative phase retardation around the optic nerve head measured by PS-SD-OCT with simple averaging (dotted line), the histogram-based method (solid line), and GDx-VCC (dashed line). The notations used on the horizontal axis are as follows: T: temporal, S: superior, N: nasal, I: inferior.

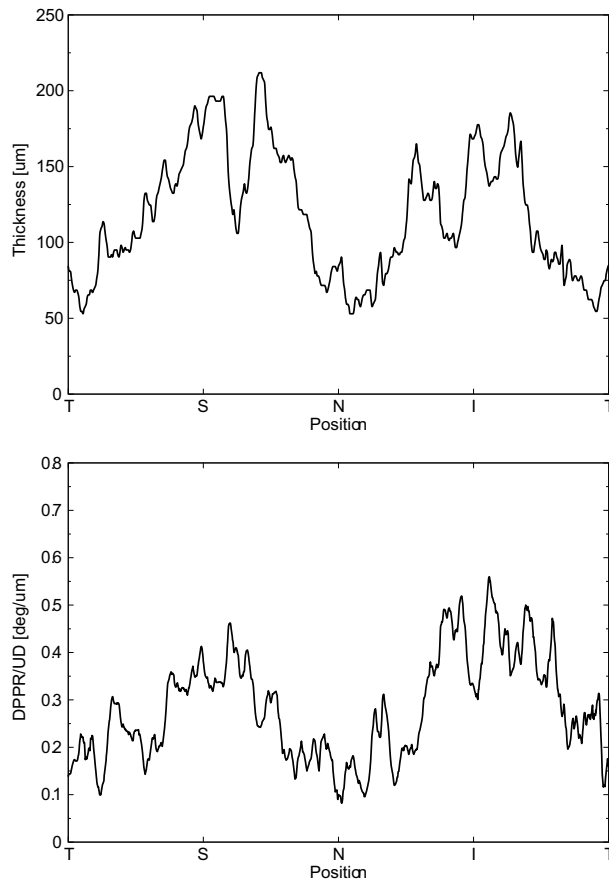


Figure 3.8: The thickness (upper graph) and DPPR/UD (lower graph) of RNFL of the healthy eye in the annular area.

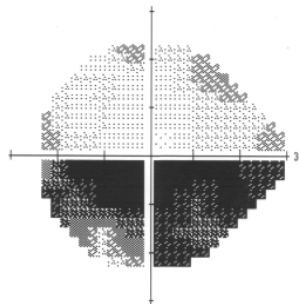


Figure 3.9: Visual field test of the glaucomatous eye measured using the Humphrey field analyzer II (Carl Zeiss Meditec) with full threshold method on the central 24 degrees of the visual field.

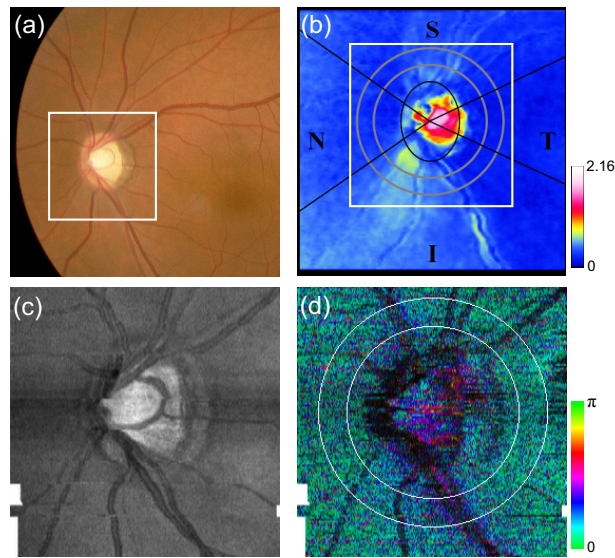


Figure 3.10: Fundus image (a), nerve fiber thickness map measured by GDx-VCC (b), *en face* projection image of the OCT intensity (c), and *en face* phase retardation image measured by PS-SD-OCT (d) for the glaucomatous eye. The fundus image was measured by a mydriatic fundus camera. The measurement range is the same as that shown in Fig. 3.6. Since the lateral quick motion in the inferior region of PS-SD-OCT images was manually compensated after the measurement, there are some empty spaces in (c) and (d).

and (d). In the inferior region, GDx-VCC had a relatively higher phase retardation at the nasal side near the optic nerve head than PS-SD-OCT. Although the superior and inferior visual fields in Fig. 3.9 showed apparent differences, it is difficult to detect such differences in Figs. 3.10 (b) and (d). A quantitative comparison provides useful results.

Figure 3.11 shows the phase retardation curves and circular intensity image of the glaucomatous eye. The agreement between the phase retardation curves of PS-SD-OCT and GDx-VCC were significantly improved by the histogram-based method, while the curve calculated by a simple rolling average was not sufficient. In both the PS-SD-OCT and GDx-VCC curves, the superior phase retardation had a lower value than that of the inferior region. Again, the phase retardation measured by PS-SD-OCT had local peaks on one side of the retinal vessels, as indicated by arrows in Fig. 3.11. The values of the phase retardation curve of GDx-VCC were close to those of the PS-SD-OCT curve, excluding the sharp peaks near the blood vessels. As we described in the previous subsection, this difference may be due to the different smoothing methods of PS-SD-OCT and GDx-VCC.

In PS-SD-OCT, the conventional three-dimensional OCT intensity volume is also acquired simultaneously with the phase retardation volume, which enables a direct structural observation of RNFL. Figure 3.12 shows the superior and inferior B-scan intensity images that are tangential

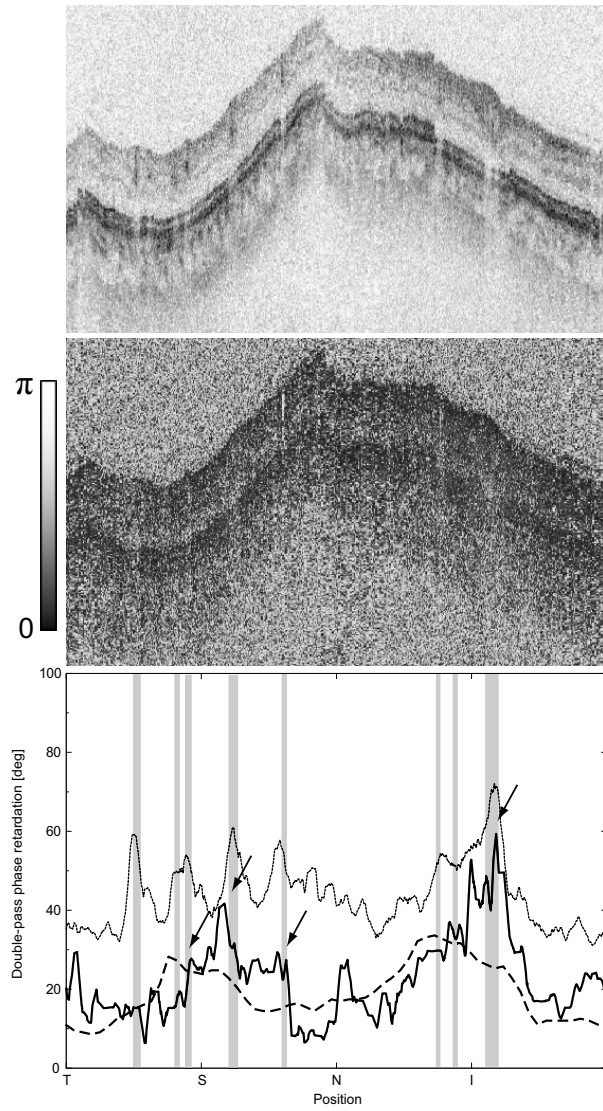


Figure 3.11: The upper image shows the OCT intensity at the center of the peripheral annular area of the glaucomatous eye. The middle image shows the phase retardation image at the same position of the upper intensity image. The axial range of these images is 0.96 mm. The lower figure shows the round-trip cumulative phase retardation around the optic nerve head measured by PS-SD-OCT with simple averaging (dotted line), the histogram-based method (solid line), and GDx-VCC (dashed line).

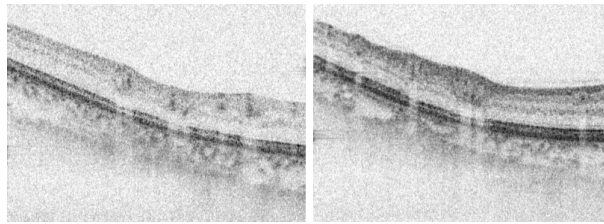


Figure 3.12: OCT B-scan images of a glaucomatous eye in the superior (left) and inferior (right) regions.

to the inner circle of radius 1.2 mm. The thinning of RNFL in the superior region was apparent, which is in agreement with the phase retardation measurements of PS-SD-OCT and GDx-VCC. The visual field test in Fig. 3.9 also supports the above mentioned results, namely, the decreased phase retardation and thinning of RNFL measured by PS-SD-OCT and GDx-VCC.

The thickness was manually segmented from the intensity image in Fig. 3.11 and DPPR/UD was calculated for the glaucomatous eye as shown in Fig. 3.13. The posterior boundary of the RNFL was not clear compared to the healthy eye. Hence, Fig. 3.13 has poor reliability. The DPPR/UD was deviated, but this is a result of the unreliable thickness. The thickness measurement has to be improved using ultrahigh resolution and a sophisticated algorithm of the segmentation for the further investigation of the birefringence of glaucomatous eyes in the future.

3.3.5 Observation of the phase retardation by polar plot

To observe the distribution of the cumulative phase retardation intuitively, the polar plot of the phase retardation curve overlaid on the *en face* phase retardation map is shown in Fig. 3.14. The center and outermost scale of the polar plot shows 0° and 100° , respectively. This polar plot shows the *en face* distribution of the phase retardation and the representative curve of the phase retardation in the annular area. The area of high phase retardation in the healthy eye broadens in both the superior and inferior regions. This representation is useful when normal and glaucomatous eyes are compared, as shown in the following paragraph.

Figure 3.15 shows the polar plot of the phase retardation of the glaucomatous eye. In contrast to the healthy eye shown in Fig. 3.14, the phase retardation of the glaucomatous eye was less both in the superior and inferior directions and the double-hump pattern was degraded. The glaucomatous eye had a relatively high phase retardation at the inferior temporal crest. In the inferior temporal crest, only PS-SD-OCT showed high phase retardation; however, GDx-VCC did not. Although the reason for this difference is not clear, PS-SD-OCT showed consistent results in the intensity images. The circular intensity image in Fig. 3.11 and the B-scan images in Fig. 3.12 showed that the RNFL was still thick in the inferior temporal area. Although the use of a polar plot is only another visualization technique, it would help understand the distribution

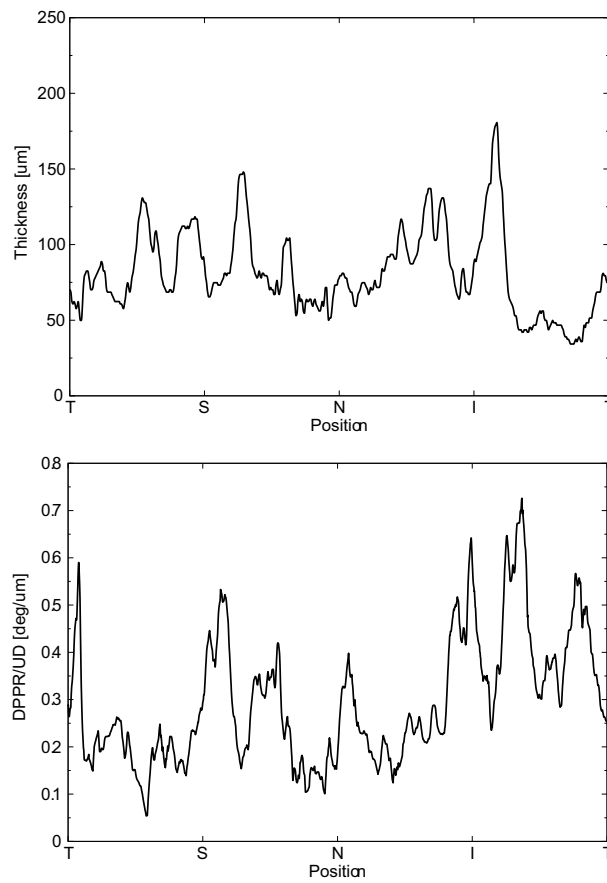


Figure 3.13: The thickness (upper graph) and DPPR/UD (lower graph) of RNFL of the glaucomatous eye in the annular area.

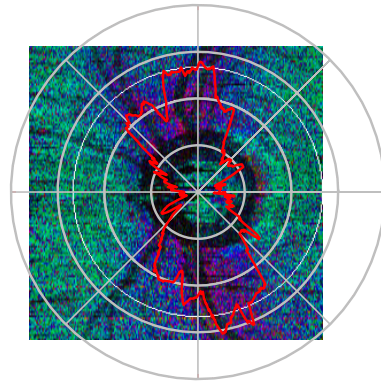


Figure 3.14: Polar plot of the TSNIT phase retardation curve over the *en face* phase retardation map of the healthy eye. The origin of the polar plot was set at the center of the annular ring used to calculate the TSNIT curve. The range of the radial axis (phase retardation) is $0-100^\circ$ with a 25° scale.

of phase retardation.

3.4 Summary

In summary, RNFL phase retardation was measured by PS-SD-OCT and GDx-VCC. In the healthy eye, both PS-SD-OCT and GDx-VCC had the double-hump pattern of RNFL. PS-SD-OCT had several peaks of the phase retardation near the retinal blood vessels. GDx-VCC also had such peaks in the *en face* phase retardation image, but they were smoothed in the phase retardation curve of the annular area. The DPPR/UD of the healthy eye measured by PS-SD-OCT was in the same order of the previously published results. In the glaucomatous eye, the double-hump pattern of RNFL was degraded in both PS-SD-OCT and GDx-VCC. The phase retardation curve measured by PS-SD-OCT also had several peaks near the retinal blood vessels. Both PS-SD-OCT and GDx-VCC had higher phase retardation of the inferior region than that of the superior region, which agreed with the visual field test. The thickness and DPPR/UD of the glaucomatous eye were less reliable than that of the healthy eye.

To our knowledge, this is the first time to compare PS-OCT and SLP quantitatively. Our results suggest that PS-SD-OCT can measure the cumulative phase retardation of RNFL as well as GDx-VCC. In addition, PS-SD-OCT has the ability to measure the thickness and birefringence of RNFL. Although the further study is required, PS-SD-OCT can potentially be used to diagnose glaucoma by using these three parameters.

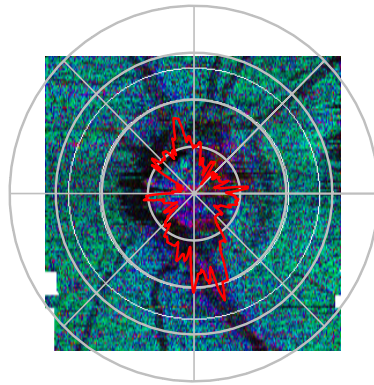


Figure 3.15: Polar plot of the TSNIT phase retardation curve over the *en face* phase retardation map of the glaucomatous eye. The scale of the polar plot is the same as that in Fig. 3.14.

Chapter 4

Fiber-based polarization-sensitive swept-source optical coherence tomography

Abstract

An improved algorithm of PS-OCT is developed for swept-source optical coherence tomography (SS-OCT). The light source is a frequency swept laser centered at $1.31 \mu\text{m}$ with a scanning rate of 20 kHz. A key point of this system is the frequency multiplexing of the polarization modulation and the wavelength sweeping. The incident polarization is modulated by a resonant electro-optic modulator at 33.3 MHz, which is one-third of the data acquisition frequency. The zeroth- and first-order harmonic components of the OCT signals with respect to the polarization modulation frequency have the polarimetric information of the sample. By algebraic and matrix calculations of the signals, this system can measure the depth-resolved Jones matrices of the sample with a single wavelength scan. Hence, a highly dense transversal scan relative to the transversal optical resolution is not required; however, it is mandatory if the algorithm uses multiple wavelength sweeping to obtain a single depth scan with polarization sensitivity. This property frees the system from the limited transversal measurement range. The phase fluctuations of the starting trigger of wavelength scan and the polarization modulation are cancelled by monitoring the OCT phase of a calibration mirror inserted into the sample arm. We demonstrate the potential of the system by performing volumetric measurements of chicken breast muscle and an *in vivo* human anterior eye segment. The phase retardation image shows an additional contrast in the fibrous tissue such as the collagen fiber in the trabecular meshwork and sclera.

4.1 Introduction

In Chapter 2, we described the PS-SD-OCT with B-scan-oriented polarization modulation. The system is based on fiber-optic components, and it measures all elements of the Jones matrix of the sample. Although the PS-SD-OCT system successfully measured biological samples, e.g., chicken breast muscle, a finger pad, a tooth, and RNFL in Chapter 3, it still had a limitation of the transversal scanning density. In addition, the polarization-sensitive spectrometer requires highly accurate alignment, which increases the difficulty to apply the system to clinical studies.

Swept-source OCT (SS-OCT) or optical frequency domain imaging (OFDI) is the other implementation of FD-OCT [7]. The light source scans the wavelength with narrow instantaneous linewidth. A photodetector detects the interference of the reference light and the backscattered light from the sample. The spectrum of the interference is recorded by a digitizer in time sequence. The post processing is similar to SD-OCT. In brief, the spectrum is rescaled to k-space in order to calibrate the nonlinearity of the wavelength scan, and Fourier transformed in order to obtain the OCT signal. When we apply a polarization sensitivity to the SS-OCT, an advantage of SS-OCT over SD-OCT is the simple implementation of the detection arm. In case of PS-SS-OCT, a polarizing beam splitter and two photodetectors are used at the detection arm. Since it does not have grating-based spectrometer, an alignment of the detection arm becomes quite simple. Hence, the configuration of PS-SS-OCT is effective to achieve a low-cost, easy-maintenance system. Another advantage of SS-OCT is the availability of frequency multiplexing over the wavelength scan of the light source. It enables an additional scan in a single wavelength scan.

In this chapter, we present a fiber-based PS-SS-OCT system based on a novel algorithm using continuous polarization modulation. The incident polarization is modulated at one-third of the frequency of the data acquisition. It generates frequency-shifted OCT signals with respect to the modulation frequency. Since this method can provide the Jones matrix of the sample with a single wavelength-scan, a highly dense scan is not required. We describe the details of the system and theory in Section 4.2 and show the intensity, phase retardation and orientation images of chicken breast muscle and an *in vivo* anterior eye segment in Section 4.3.

4.2 System and theory

4.2.1 System configuration

Figure 4.1 shows the schematic of the system. The light source is a commercially available scanning laser (HSL-2000, Santec, Japan). A standard SS-OCT system with this light source was reported previously [74]. The light source sweeps the wavelength at a line rate of 20 kHz over a span of 110 nm centered at 1.31 μm . The output power is 5.4 mW, and the lasing duty cycle is 50%. The light is polarized by a linear polarizer (LP) at 90° and modulated by a resonant electro-optic modulator (EOM) with an optic axis of 45° (EO-AM-R-033.3-C3, Nova Phase,

Inc). The EOM sinusoidally modulates the phase retardation between the horizontal and vertical polarizations of light at a frequency of 33.3 MHz and a modulation amplitude of 2.405 radians. A function generator (33250A, Agilent Inc) and an RF amplifier (RFAMP-150, Nova Phase, Inc) with a voltage gain of 25.5 dB drive the EOM. The modulated light is coupled to a single mode fiber coupler. 10% of this modulated light is directed to the reference arm and 90% to the sample arm. In the reference arm, in-line polarization controllers (PC) and an LP have a role in obtaining a constant optical power and a constant state of polarization at the reference arm independent of the incident polarization modulation by the EOM. For this purpose, a photodetector connected to an oscilloscope in the reference arm monitors the optical power, and is utilized in aligning of the PCs and LP. The reference light is then coupled to a polarization-maintaining fiber (PMF). In the sample arm, 99% of the light illuminates the sample through a two-axis galvanometer scanner and an objective lens with a 60 mm focal length. The theoretical transversal resolution at the focus is 32.2 μm . 1% of the probing light is directed to a mirror in order to provide a calibration signal for the timing-phase difference between the EOM and the data acquisition of each spectral acquisition. The details of this active calibration are described in Section 4.2.3. Back-reflected light from the sample arm is coupled to the PMF. The reference and sample beams are directed to a polarization-maintaining fiber coupler (PMC) and interfered with each other. In-line fiber-optic polarizing beamsplitters (PBSs) are attached to the two output ports of the PMC. The horizontally and vertically polarized signals are detected by two balanced photoreceivers (Model 1817, New Focus, Inc.). The detected signals are bandpass filtered from 300 kHz to 55 MHz and amplified electrically. A data acquisition board (Octopus CS8349, Gage Applied Technologies, Inc.) acquires the data at 100 MS/s.

4.2.2 Principle of polarization-sensitive detection

In this subsection, we first describe the polarization in the system using the Jones formalism. Then, we derive the birefringence of the sample.

The phase modulation of the EOM is

$$\varphi = A_0 \sin(\omega_m t), \quad (4.1)$$

where $A_0 = 2.405$ radians and ω_m is the frequency of the polarization modulation. The Jones matrix of the EOM with the fast axis of $\pi/4$ can be written as

$$\begin{pmatrix} \cos \frac{\varphi}{2} & i \sin \frac{\varphi}{2} \\ i \sin \frac{\varphi}{2} & \cos \frac{\varphi}{2} \end{pmatrix}. \quad (4.2)$$

By applying Eq. (4.2) to the Jones vector of the vertically polarized light, the Jones vector of the light after the modulation by the EOM is derived as

$$\begin{pmatrix} H_i \\ V_i \end{pmatrix} = \begin{pmatrix} i \sin \frac{\varphi}{2} \\ \cos \frac{\varphi}{2} \end{pmatrix}. \quad (4.3)$$

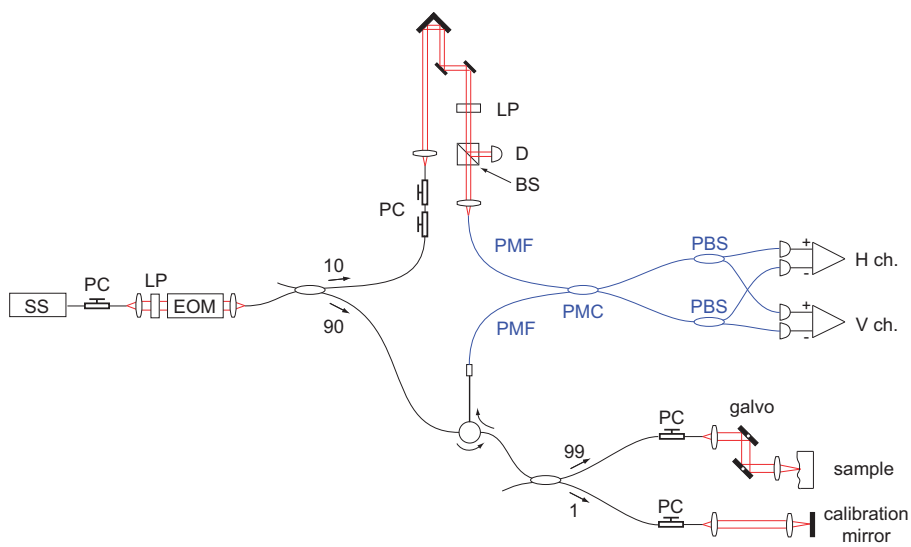


Figure 4.1: Schematic of the system. SS: frequency swept laser source, PC: in-line polarization controller, LP: linear polarizer, EOM: electro-optic modulator, D: photodetector, BS: nonpolarizing beamsplitter, PMF: polarization-maintaining fiber, PMC: polarization-maintaining coupler, PBS: in-line fiber-optic polarizing beamsplitter, H ch.: balanced photoreceiver of horizontally polarized light channel, V ch.: balanced photoreceiver of vertically polarized light channel.

We define the Jones matrix that accounts for the birefringence of the fiber-optic components and the sample as

$$\mathbf{J}_{\text{all}} = \mathbf{J}_{\text{out}}\mathbf{J}_{\text{sam}}\mathbf{J}_{\text{in}} = \begin{pmatrix} j_{1,1} & j_{1,2} \\ j_{2,1} & j_{2,2} \end{pmatrix}, \quad (4.4)$$

where \mathbf{J}_{in} is a Jones matrix from the EOM to the sample surface, \mathbf{J}_{sam} is a depth-dependent double-pass Jones matrix of the sample, which we want to determine, and \mathbf{J}_{out} is a Jones matrix from the sample surface to the PMC. The Jones vector of light from the sample at the PMC can be represented as

$$\begin{pmatrix} H_{\text{sam}} \\ V_{\text{sam}} \end{pmatrix} = \mathbf{J}_{\text{all}} \begin{pmatrix} H_i \\ V_i \end{pmatrix} = \begin{pmatrix} j_{1,2} \cos \frac{\varphi}{2} + ij_{1,1} \sin \frac{\varphi}{2} \\ j_{2,2} \cos \frac{\varphi}{2} + ij_{2,1} \sin \frac{\varphi}{2} \end{pmatrix} \quad (4.5)$$

The Jones vector of the reference light at the PMC can be represented as

$$\mathbf{E}_{\text{ref}} = \begin{pmatrix} H_{\text{ref}} \\ V_{\text{ref}} \end{pmatrix} = \begin{pmatrix} H_r \\ V_r \end{pmatrix} e^{-i\frac{\varphi}{2}}, \quad (4.6)$$

where H_r and V_r represent the phase constants without the polarization modulation. The horizontally polarized component of the interference signal of the reference and sample beams at the detection arm is

$$I_h(t) = |H_{\text{ref}}|^2 + |H_{\text{sam}}|^2 + H_{\text{ref}}(t)H_{\text{sam}}^*(t) + c.c., \quad (4.7)$$

where *c.c.* denotes the complex conjugate of the third term. The first and second terms are suppressed by the balanced photoreceiver. The third and *c.c.* terms represent the OCT signal and its mirror corresponds to the positive and negative frequency components of the spectral interference signal. The path length of the reference arm is adjusted so that the positive and negative frequency terms of the OCT signal do not overlap with each other in the axial depth range. Therefore, we consider only the third term in the following equations. The detected signal $I_h(t)$ is Fourier transformed and rearranged as

$$\tilde{I}_h(\tilde{t}) = \mathcal{F}[H_{\text{ref}}(t)H_{\text{sam}}^*(t)] = \frac{H_r}{2} \{ \mathcal{F}[j_{1,2}^* - j_{1,1}^*] + \mathcal{F}[j_{1,2}^* + j_{1,1}^*] * \mathcal{F}[e^{-i\varphi}] \}, \quad (4.8)$$

where \tilde{I}_h denotes the interference part of the signal, \tilde{t} is the Fourier conjugate of t , and $\mathcal{F}[\cdot]$ and $*$ denote the Fourier transform from time to its Fourier spectral domain and a convolution operator, respectively. Here, we have to note that the spectral interference signal obtained is not rescaled to the optical frequency domain. This is because the polarization modulation of the probe beam is even in the sampling timing. The second term was shifted in the \tilde{t} domain because of the polarization modulation by the EOM. $\mathcal{F}[e^{-i\varphi}]$ can be rearranged as

$$\begin{aligned} \mathcal{F}[e^{-i\varphi}] = & \sum_{l=0}^{\infty} [J_{2l}(A_0) \{ \delta(k - 2l\omega_m) + \delta(k + 2l\omega_m) \} \\ & - J_{2l+1}(A_0) \{ \delta(k - (2l+1)\omega_m) + \delta(k + (2l+1)\omega_m) \}], \end{aligned} \quad (4.9)$$

using the expansion of the Bessel functions to the trigonometric terms,

$$\begin{cases} \sin[\varphi(t)] = \sum_{l=0}^{\infty} 2J_{2l+1}(A_0) \sin[(2l+1)\omega_m t] \\ \cos[\varphi(t)] = J_0(A_0) + \sum_{l=1}^{\infty} 2J_{2l}(A_0) \cos[(2l)\omega_m t] \end{cases} \quad (4.10)$$

where the italicized capital letters $J_0(A_0)$, $J_{2l}(A_0)$, and $J_{2l+1}(A_0)$ are the Bessel functions of the first kind of the order of 0, $2l$, and $2l+1$, respectively. Since we set $A_0 = 2.405$ radians, the zeroth-order Bessel function disappears, namely, $J_0(A_0) = 0$. Equations (4.8) and (4.9) suggest that the zeroth ($l = 0$) and first ($l = 1$) order terms are distinctive in the Fourier-spectrum space, and we can distinguish these two signals as

$$\tilde{I}_{h0}(z) = \frac{H_r}{2}(j_{1,2}^* - j_{1,1}^*), \quad (4.11)$$

$$\tilde{I}_{h1}(z) = -\frac{J_1(A_0)H_r}{2}(j_{1,2}^* + j_{1,1}^*), \quad (4.12)$$

where $\tilde{I}_{h0}(z)$ and $\tilde{I}_{h1}(z)$ are the zeroth- and first-order horizontally polarized OCT signals, respectively.

Figure 4.2 shows the schematic diagram of the detected signal in the Fourier-spectral domain. Since the detected signals are of real values, the zeroth-order signal has positive and negative frequency components close to the zero depth. The polarization modulation generates the \pm first-order signals with respect to the frequency of the EOM (the negative first-order signal is not shown in Fig. 4.2). The zeroth- and first-order complex signals correspond to the first row of the Jones matrix as shown in Eqs. (4.11) and (4.12). In the Fourier-spectral domain shown in Fig. 4.2, they are windowed and extracted individually. The first-order signal is then shifted so that the frequency of the polarization modulation is demodulated. The zeroth-order and the shifted first-order signals are individually inverse Fourier transformed to the original detection domain, which results in complex interference spectra. The real and imaginary parts of the complex spectra of the zeroth- and first-order signals are individually rescaled in order to calibrate the nonlinearity of the frequency sweeping of the light source. Finally, two complex spectral interference signals linearly tuned in the optical frequency are obtained.

When the path lengths of the PMF in the reference and sample arms are different, there arises a difference between the path lengths of horizontally and vertically polarized OCT signals. This is because the refractive indices of horizontally and vertically polarized modes in the PMF are different. It is compensated for by accuracy higher than a single pixel through the numerical adjustment of the first-order dispersions to the horizontally and vertically polarized spectra individually. The remaining path-length mismatch between the horizontally and vertically polarized OCT signals results in the constant phase accounted by H_r and V_r . Hence, we can safely ignore it, as described later.

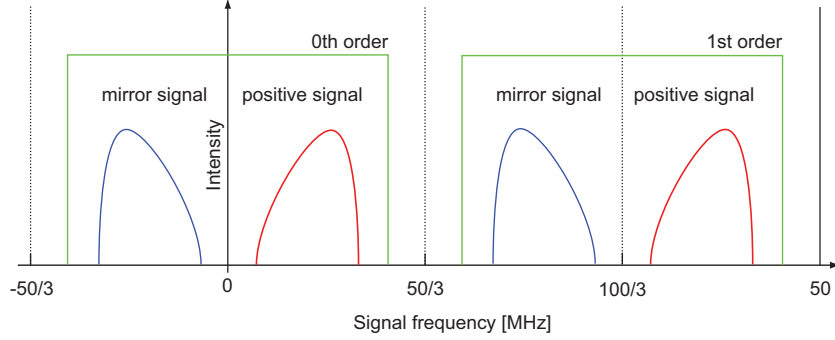


Figure 4.2: Diagram of the detected signal after Fourier transform.

The mismatch of the second-order dispersion between the reference arm and the sample arm is compensated numerically for all spectra. The compensated spectra are Fourier transformed, and the depth-resolved signals $\tilde{I}_{h0}(z)$ and $\tilde{I}_{h1}(z)$ are obtained.

In our implementation, the signal stability of the first-order negative signal is higher than that of the first-order positive signal because of the noise properties of the system. Therefore, the zeroth- and first-order negative signals are used for the calculation.

Equations (4.11) and (4.12) are rearranged in order to obtain two elements of the Jones matrix \mathbf{J}_{all} as

$$H_r j_{1,1}^* = - \left(\tilde{I}_{h0} + \frac{\tilde{I}_{h1}}{J_1(A_0)} \right), \quad (4.13)$$

$$H_r j_{1,2}^* = \tilde{I}_{h0} - \frac{\tilde{I}_{h1}}{J_1(A_0)}. \quad (4.14)$$

In the same manner, the other two elements of the Jones matrix can be calculated using the vertically polarized signals as

$$V_r j_{2,1}^* = - \left(\tilde{I}_{v0} + \frac{\tilde{I}_{v1}}{J_1(A_0)} \right), \quad (4.15)$$

$$V_r j_{2,2}^* = \tilde{I}_{v0} - \frac{\tilde{I}_{v1}}{J_1(A_0)}. \quad (4.16)$$

We obtain the Jones matrix $\mathbf{J}_{\text{measured}}$ by combining Eqs. (4.13), (4.14), (4.15), and (4.16) as

$$\mathbf{J}_{\text{measured}} = \begin{pmatrix} H_r^* & 0 \\ 0 & V_r^* \end{pmatrix} \begin{pmatrix} - \left(\tilde{I}_{h0}^* + \frac{\tilde{I}_{h1}^*}{J_1(A_0)} \right) & \tilde{I}_{h0}^* - \frac{\tilde{I}_{h1}^*}{J_1(A_0)} \\ - \left(\tilde{I}_{v0}^* + \frac{\tilde{I}_{v1}^*}{J_1(A_0)} \right) & \tilde{I}_{v0}^* - \frac{\tilde{I}_{v1}^*}{J_1(A_0)} \end{pmatrix}. \quad (4.17)$$

We set the LP and PC in the reference arm in order to satisfy the condition $|H_r| = |V_r|$. Hence, we can omit the amplitudes of the first matrix on the right-hand side of Eq. (4.17). It is arranged

as

$$\mathbf{J}_{\text{offset}} = \begin{pmatrix} 1 & 0 \\ 0 & e^{i\gamma} \end{pmatrix}, \quad (4.18)$$

where $e^{i\gamma} = \angle(V_r^*) - \angle(H_r^*)$. $\mathbf{J}_{\text{offset}}$ describes the constant phase offset between the horizontally and vertically polarized signals due to an effect of the PMF in the reference and sample arms. Equation (4.18) is clearly a unitary matrix. The measured Jones matrix can be described as

$$\mathbf{J}_{\text{measured}} = \mathbf{J}_{\text{offset}} \mathbf{J}_{\text{all}}. \quad (4.19)$$

Assuming that fiber-optic components have no diattenuation, \mathbf{J}_{in} and \mathbf{J}_{out} can be characterized as elliptic retarders, namely, unitary matrices. In order to compensate the effects of the fiber-optic components, namely, \mathbf{J}_{in} , \mathbf{J}_{out} and $\mathbf{J}_{\text{offset}}$, we apply the matrix diagonalization method developed by Park et al. [39] These procedures finally provide the phase retardation, diattenuation, and relative orientation of the sample.

4.2.3 Calibration of phase fluctuation

Since the PS-SS-OCT is a phase-sensitive system, the phase fluctuation results in an artifact of the measurement. The sources of the phase fluctuation are the jitter of the start trigger of the wavelength sweeping generated by the light source, which we define as A-trigger, and the asynchronous driving between the data acquisition and the polarization modulation by the EOM. In this subsection, we describe how they affect the system and how they can be cancelled.

The DAQ receives an A-trigger from the light source and starts the acquisition. The A-trigger has a fluctuation in the timing because it is generated by a photodetector equipped with a narrow optical bandpass filter and is not sufficiently accurate to be synchronized with the timing clock of the DAQ. The A-trigger fluctuation in successive A-scans causes the phase error among the OCT signals that linearly increases to the axial depth. Both zeroth- and first-order OCT signals are affected by the same phase error. Vakoc et al. have developed a method to compensate the A-trigger fluctuation [75]. In their method, a calibration mirror in the sample arm is used as a phase reference. We apply a modified version of their method to our system.

According to the shift theorem of the Fourier transform, the phase error can be written as $\exp\{-i2\alpha z \varepsilon(n)\}$, where α is the wavenumber-sweeping rate of the light source ($-1.6 \cdot 10^{10} \text{ m}^{-1} \text{ s}^{-1}$) and $\varepsilon(n)$ is the acquisition timing offset of the n -th A-scan. The zeroth-order horizontally polarized OCT signal \tilde{I}_{h0} is then rewritten as $\exp\{-i2\alpha z \varepsilon(n)\} \tilde{I}_{h0}$. The other OCT signals \tilde{I}_{h1} , \tilde{I}_{v0} , and \tilde{I}_{v1} are also affected by the same phase fluctuation. From Eq. (4.17), the phase error is common for all elements of \mathbf{J}_{all} , namely,

$$\mathbf{J}'_{\text{measured}} = e^{i2\alpha z \varepsilon(n)} \mathbf{J}_{\text{measured}} = e^{i2\alpha z \varepsilon(n)} \mathbf{J}_{\text{offset}} \mathbf{J}_{\text{all}}. \quad (4.20)$$

Hence, the A-trigger fluctuation does not change any property of $\mathbf{J}'_{\text{measured}}$ in the sense of a Jones matrix.

The second source of the phase fluctuation is the phase difference between the DAQ and the EOM. The light source has a polygon mirror scanner and the EOM is driven by a resonant electric circuit. Since these devices cannot be controlled externally during the resonant driving, it is difficult to synchronize them. Therefore, they are not synchronized in our system. This induces a phase offset to the polarization modulation. Equation (4.1) is rewritten as

$$\varphi' = A_0 \sin(\omega_m t - \delta(n)), \quad (4.21)$$

where $\delta(n)$ is the phase offset of the n -th A-scan. Subsequently, equation (4.8) is rewritten as

$$\tilde{I}_h(z) = \frac{H_r}{2} \{ \mathcal{F}[j_{1,2}^* - j_{1,1}^*] + e^{i\delta(n)} \mathcal{F}[j_{1,2}^* + j_{1,1}^*] * \mathcal{F}[e^{-i\varphi}] \}. \quad (4.22)$$

Equation (4.22) shows that the phase offset of the polarization modulation causes a depth-independent phase offset of the first-order signal. From Eqs. (4.17) and (4.20), the measured Jones matrix can be rewritten and rearranged to factorize the term involving $\delta(n)$ as

$$\begin{aligned} \mathbf{J}_{\text{measured}}'' &= e^{i2\alpha z \varepsilon(n)} \mathbf{J}_{\text{offset}} \begin{pmatrix} - \left(\tilde{I}_{h0}^* + \frac{e^{-i\delta(n)} \tilde{I}_{h1}^*}{J_1(A_0)} \right) & \tilde{I}_{h0}^* - \frac{e^{-i\delta(n)} \tilde{I}_{h1}^*}{J_1(A_0)} \\ - \left(\tilde{I}_{v0}^* + \frac{e^{-i\delta(n)} \tilde{I}_{v1}^*}{J_1(A_0)} \right) & \tilde{I}_{v0}^* - \frac{e^{-i\delta(n)} \tilde{I}_{v1}^*}{J_1(A_0)} \end{pmatrix} \\ &= e^{i2\alpha z \varepsilon(n)} \mathbf{J}_{\text{offset}} \mathbf{J}_{\text{all}} \mathbf{J}_{\text{offset}2}, \end{aligned} \quad (4.23)$$

where

$$\mathbf{J}_{\text{offset}2} = \frac{1}{2} \begin{pmatrix} e^{-i\delta(n)} + 1 & e^{-i\delta(n)} - 1 \\ e^{-i\delta(n)} - 1 & e^{-i\delta(n)} + 1 \end{pmatrix}. \quad (4.24)$$

Note that Eq. (4.24) is a unitary matrix.

Equation (4.23) shows that the A-trigger fluctuation and phase difference between the DAQ and the EOM induce the depth-dependent global phase offset and the depth-independent unitary matrix. They have limited effects to the measured Jones matrix, because they generate no artifact after the matrix diagonalization for a single A-scan.

If the surface Jones matrix is extracted from each depth scan, the speckle noise of the sample surface significantly degrades the phase retardation and orientation images because of the failure of the matrix diagonalization. To overcome this problem, the surface Jones matrices have to be averaged. However, the averaging is not possible because of the phase fluctuation. In addition, we cannot remove the fixed pattern noise numerically. Therefore, we should compensate them.

To compensate the phase difference between DAQ and EOM, first we calculate the relative phase difference of the OCT signals from the calibration mirror between the zeroth and n -th A-scans,

$$e^{i\{\delta(n)-\delta(0)\}} = \left\{ \frac{e^{i\delta(n)} e^{-i2\alpha z \varepsilon(n)} \tilde{I}_{h1}}{e^{-i2\alpha z \varepsilon(n)} \tilde{I}_{h0}} \right\} / \left\{ \frac{e^{i\delta(0)} e^{-i2\alpha z \varepsilon(0)} \tilde{I}_{h1}}{e^{-i2\alpha z \varepsilon(0)} \tilde{I}_{h0}} \right\}. \quad (4.25)$$

The n -th A-scan is divided by Eq. (4.25) in order to eliminate $\delta(n)$ as

$$\frac{1}{e^{i\{\delta(n)-\delta(0)\}}} e^{i\delta(n)} e^{-i2\alpha z \varepsilon(n)} \tilde{I}_{h1} = e^{i\delta(0)} e^{-i2\alpha z \varepsilon(n)} \tilde{I}_{h1}. \quad (4.26)$$

To compensate the A-trigger fluctuation, we can use the zeroth-order calibration signal, because the zeroth-order signal is affected only by the A-trigger fluctuation. The counter phase is generated based on the zeroth-order calibration signal and is applied to all the OCT signals of \tilde{I}_{h0} , \tilde{I}_{h1} , \tilde{I}_{v0} , and \tilde{I}_{v1} . As a result, the zeroth- and first-order OCT signals are compensated as $\exp\{-i2\alpha z\varepsilon(0)\}\tilde{I}_{h0}$ and $\exp\{i\delta(0)\}\exp\{-i2\alpha z\varepsilon(0)\}\tilde{I}_{h1}$, respectively.

In practice, the A-trigger fluctuation is greater than one sampling time of the DAQ, approximately five sampling times (50 ns), due to the limited accuracy of the A-trigger generator equipped with the light source. This results in the phase wrapping ambiguity of the correction by the calibration mirror, because it locates at the deep position. Instead of a more accurate but expensive A-trigger source, such as what uses a fiber Bragg grating, we use a fixed pattern signal at a depth of 0.2 mm for a rough calibration of the A-trigger fluctuation. Subsequently, we use the calibration mirror at the deep position (3.7 mm) for a fine calibration. This two-step method can sufficiently calibrate the A-trigger fluctuation, which cannot be done with only a single calibration signal.

We measured a static mirror as a sample to confirm the calibration of the phase fluctuations. The probing light was attenuated by a neutral density filter. The galvanometer scanner was turned off. The sample and calibration mirror were placed at depths of 1.9 mm and 3.7 mm, respectively. The OCT signals \tilde{I}_{h0} and \tilde{I}_{h1} of the calibration mirror with signal-to-noise ratios (SNRs) of 33.2 dB and 26.8 dB, respectively, were used to cancel the phase fluctuations. The signal phases of 512 A-lines were acquired at the depth of the sample. The standard deviations of the phases of \tilde{I}_{h0} , \tilde{I}_{v0} , \tilde{I}_{h1} , and \tilde{I}_{v1} of the sample were 0.040, 0.042, 0.055, and 0.055 (rad) with SNRs of 41.4, 36.4, 32.1, and 33.8 (dB), respectively. The standard deviations of the phase differences between two adjacent A-lines of \tilde{I}_{h0} , \tilde{I}_{v0} , \tilde{I}_{h1} , and \tilde{I}_{v1} of the sample were 0.016, 0.023, 0.062, and 0.059 (rad), respectively. This result is within the same order as that of the results of previous studies on phase-resolved SS-OCT systems [75, 76].

At this point, the phase fluctuations among each A-scan were cancelled, and only a constant phase offset remains. Equation (4.23) becomes identical for all A-scans. As a result, the effects of the phase fluctuations are cancelled by this calibration. After the calibration, the surface Jones matrices are averaged and applied to all the A-scans in the process of matrix diagonalization. The spectra of the fixed pattern noise are obtained by averaging the spectra of \tilde{I}_{h0} , \tilde{I}_{h1} , \tilde{I}_{v0} , and \tilde{I}_{v1} individually, and the former spectra are removed from the original spectra.

The schemes of the signal processing of PS-SS-OCT is summarized in a diagram shown in Fig. 4.3.

4.3 Results

4.3.1 Measurements of a quarter-wave plate and linear polarizer

In order to test the system after the calibration, a quarter-wave plate (QWP) and an LP were measured. The orientation was rotated from 0° to 180° with a 10° increment, and 128 A-scans were

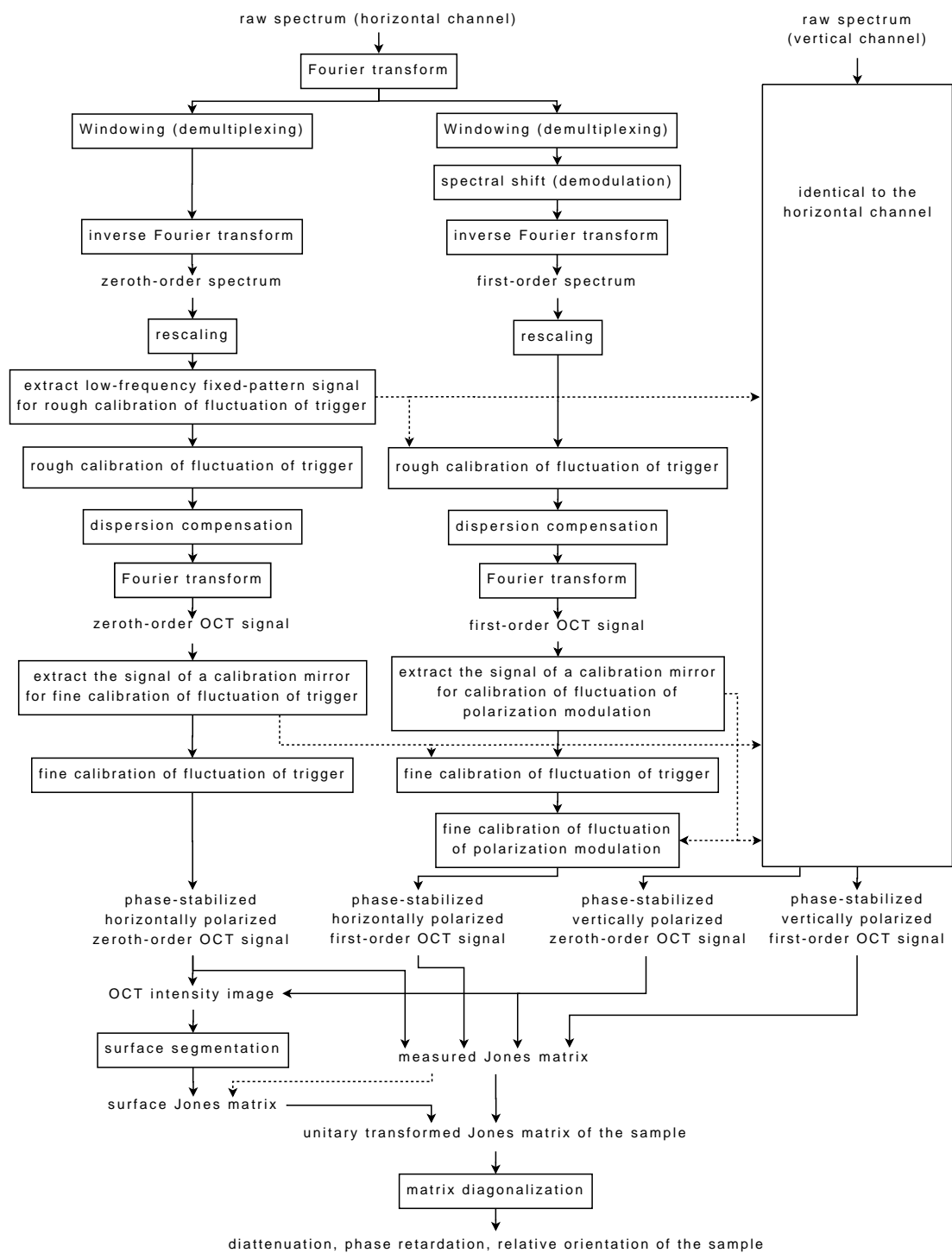


Figure 4.3: Flowchart of the data processing. Since the process of the vertically polarized channel is almost the same as that of horizontally polarized channel, its description is abbreviated.

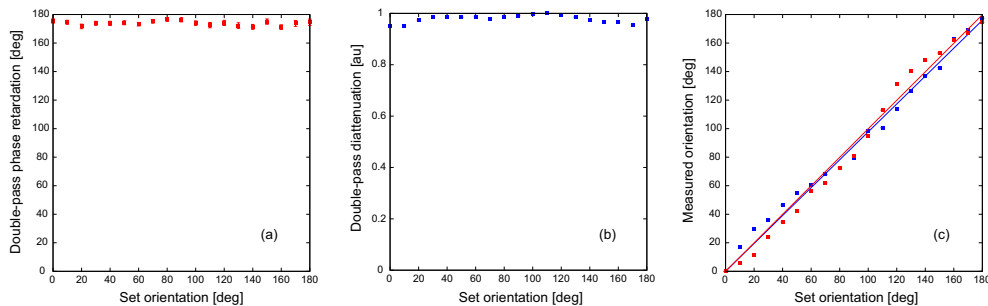


Figure 4.4: (a) Double-pass phase retardation of the QWP, (b) double-pass diattenuation of the LP, and (c) relative orientation of the QWP and LP.

averaged for each measurement. Figures 4.4 (a) and (b) show the double-pass phase retardation of the QWP and the double-pass diattenuation of LP, respectively. The averaged double-pass phase retardation of the QWP was $174 \pm 2^\circ$ and the averaged double-pass diattenuation of the LP was 0.97 ± 0.01 . They were slightly lower than the expected values because of the wrapping effect of the noise near the edge of the range. The orientation relative to 0° is shown in Fig. 4.4 (c). The least squares fitted slopes of the QWP and LP were 0.99 ± 0.01 and 0.97 ± 0.01 , respectively. The expected and measured orientations were in good agreement.

4.3.2 Measurements of biological samples

To demonstrate the potential of the system, we performed an *in vitro* measurement of chicken breast muscle. The three-dimensional intensity, phase retardation, and orientation images are shown in Fig. 4.5. A transversal scanning range of 1.6 cm was imaged with 512 axial scans. The intensity image with polarization diversity was calculated as $20 \log \left\{ \left(|\tilde{I}_{h0}| + |\tilde{I}_{v0}| \right) \right\}$. The fixed pattern noise, including the calibration mirror, was obtained by averaging the spectra in a B-scan image and it was removed from the image. Since the averaged surface Jones matrix was used as a reference to cancel the birefringence of the fiber-optic components, the phase retardation was zero at the surface of all B-scans. The phase retardation cyclically changed along the depth. The orientation had abrupt 90° shifts due to the phase wrapping at 180° phase retardation [53]. These images indicate that the system can measure the birefringence of the biological sample in the entire imaging range.

An *in vivo* human anterior eye segment was imaged by the system. Figure 4.6 shows the horizontally scanned images of the anterior chamber angle at the temporal side of an *in vivo* human right eye. The transversal scanning range of 5.0 mm (horizontal) \times 4.7 mm (vertical) was imaged with 512×237 A-lines, where the fast scan was oriented in the horizontal direction and the slow scan in the vertical direction. The intensity image showed the corneal limbus, anterior chamber angle, iris, and sclera. The phase retardation image showed a highly birefringent area with approximately total 2π phase retardation (arrow). This feature was maintained in all the

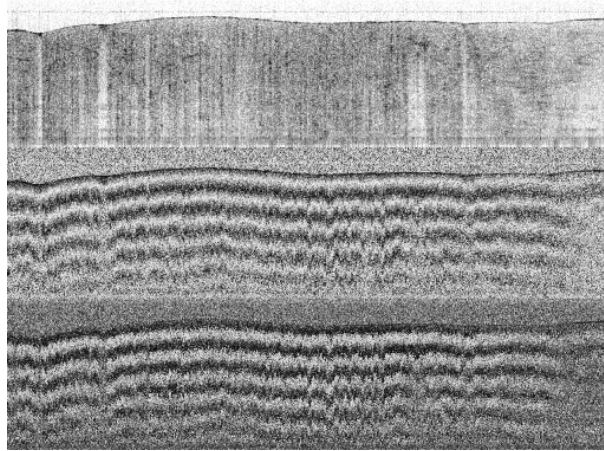


Figure 4.5: Intensity (upper), phase retardation (middle) and orientation (lower) images of the chicken breast muscle. The image size is 1.6 cm (transversal) \times 4.0 mm (axial) in air. The phase retardation image and the orientation image are indicated in gray scale from black (0°) to white (180° and 90° , respectively).

B-scans. According to our anatomical knowledge, we believe that this area corresponds to the trabecular meshwork, which has an important role in draining the aqueous flow. The cumulative phase retardation of the cornea and trabecular meshwork was projected on the iris. The projected phase retardation did not change in the iris, except in the iris pigment epithelium (IPE). The phase retardation of IPE was random and not consistent with the above region of the iris. The random appearance of birefringence, i.e., the so-called polarization scrambling, was clearly visible in the movie because the phase retardation did not have a correlation among the successive frames. Scleral birefringence was clearly observed in all the B-scans. These features of the phase retardation are in good agreement with those of a previous study conducted by Pircher et al. using time-domain PS-OCT [77].

4.4 Discussion

Our PS-SS-OCT system can measure the Jones matrices of the sample with a long transversal range without a highly dense scan. The algorithm was similar to the time-domain PS-OCT with continuous source polarization modulation [41] and the PS-SD-OCT with B-scan-oriented polarization modulation [45], except the frequency multiplexed detection of two polarization channels based on the continuous polarization modulation.

In our PS-SS-OCT system, the polarization-modulated light was fed into both the reference and sample arms. A different optical configuration would be possible by inserting the EOM into the sample arm. In this case, the same algorithm is applicable if we double the modulation volt-

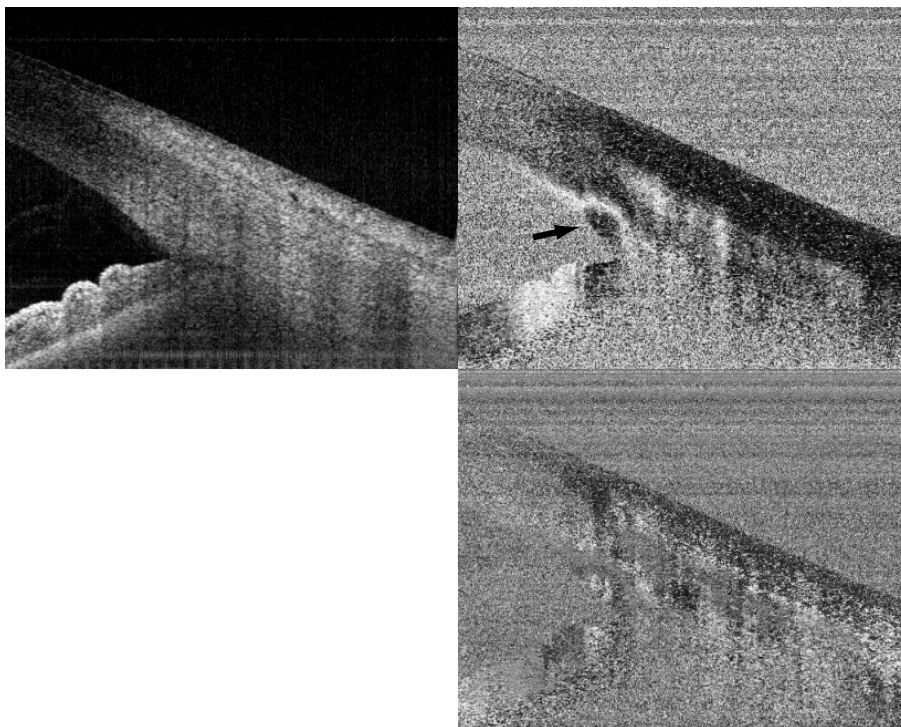


Figure 4.6: Intensity (upper left), phase retardation (upper right) and orientation (lower right) images of the *in vivo* human anterior eye segment. The size of the images was 5.0 mm \times 3.9 mm in air.

age applied to the EOM. Although we have not employed this configuration due to a limitation in the RF amplifier, it is beneficial because the calibration of the PC and monitoring of the optical power in the reference arm are not required.

In the current setup, the depth range was shortened to one-third of the conventional SS-OCT. A direct method for extending the depth range is to increase the sampling frequency of the AD conversion. The other way is to optimize the modulation frequency. We can set the frequency of the polarization modulation at the Nyquist frequency of the data acquisition and suppress the first-order positive frequency image by a sharp electric low-pass filter. The remaining first-order negative frequency image can be used for processing the Jones matrix. With this configuration, the depth range can be extended up to half of what is achieved by the conventional SS-OCT. In this study, we use a sufficient margin to measure the entire first-order OCT signal.

When the sample is illuminated by 2.0-mW probing light and the backscattered light from the sample is evenly detected by the two photodetectors, the theoretical shot-noise-limited sensitivity [7] without polarization modulation is 115.2 dB. Assuming that there is no birefringence of the fiber-optic components and the sample and no phase fluctuation, the sensitivity of the zeroth-order OCT signal drops at -6 dB, which results in a sensitivity of 109.2 dB. The measured sensitivity is 101.7 dB at the depth of 566 μm . A dominant factor of the difference between the theoretical and measured values was probably the relative intensity noise due to an incomplete suppression by the balanced detection [78].

4.5 Summary

We have demonstrated that fiber-based PS-SS-OCT can be performed with continuous source polarization modulation. By extracting the zeroth-order and first-order OCT signals with respect to the frequency of the polarization modulation, the Jones matrix of the sample is measured with a single A-scan. The calibration method for canceling the phase fluctuations from the A-trigger and the timing between the data acquisition and the polarization modulation has been developed. The imaging of the anterior eye segment shows the ability of PS-SS-OCT to provide additional contrast that could not be imaged by conventional SS-OCT.

Chapter 5

Conclusion

In this dissertation, we have developed fiber-based PS-OCT systems. A PS-SD-OCT system was developed at 840 nm. The polarization-sensitive spectrometer was aligned so that the artificial phase is minimized. A method of B-scan-oriented polarization modulation was developed. High imaging speed and three-dimensional measurement of the phase retardation was achieved for *ex vivo* and *in vivo* biological samples. The phase retardation images of chicken breast muscle, a finger pad, and caries lesion of a tooth showed the additional contrasts of the fibrous tissue.

The high-speed and highly-sensitive PS-SD-OCT system enabled the visualization of three-dimensional phase retardation image of RNFL *in vivo*. *En face* phase retardation maps of RNFL was measured by PS-SD-OCT and GDx-VCC. The double-hump pattern of RNFL of the healthy eye was observed by both systems. The DPPR/UD was calculated using the thickness and the cumulative phase retardation measured by PS-SD-OCT. The DPPR/UD measured by PS-SD-OCT was in good agreement with the previous reports. The glaucomatous eye also had similar *en face* phase retardation maps of PS-SD-OCT and GDx-VCC. Manual segmentation of the thickness of RNFL was not reliable for the glaucomatous eye, which resulted in unreliable result of the DPPR/UD. Improvement of segmentation method and axial resolution would help further study of glaucoma. The *en face* phase retardation map, the B-scan intensity images of PS-SD-OCT, and the visual field test had the consistent result. Our result suggested that the PS-SD-OCT might have a possibility to diagnose glaucoma using the intensity, cumulative phase retardation, and the birefringence of RNFL.

Fiber-based PS-SS-OCT with continuous source polarization modulation was developed at 1.3 μm . All elements of Jones matrices was calculated using a single wavelength scan without restriction of the transversal scanning density. Arbitrary transversal scanning range can be set in this system. The phase retardation image of the anterior eye segment revealed the birefringence of trabecular meshwork, which would be important to see the relation with the function of the trabecular meshwork.

We showed that both PS-SD-OCT and PS-SS-OCT systems could measure birefringence of the sample with high imaging speed and high sensitivity. In addition to applications for RNFL

and anterior eye segment, another promising applications of PS-OCT for age-related macular degeneration and photo-aged skin were demonstrated by Miura et al. and Sakai et al., respectively [79, 80]. PS-OCT would have further applications in extensive clinical researches related to fibrous tissues. For the further study and to prove the diagnostic performance, more volunteers and patients have to be measured and analyzed statistically.

Bibliography

- [1] D. Huang, E. A. Swanson, C. P. Lin, J. S. Schuman, W. G. Stinson, W. Chang, M. R. Hee, T. Flotte, K. Gregory, C. A. Puliafito, and J. G. Fujimoto, “Optical coherence tomography,” *Science* **254**, 1178–1181 (1991).
- [2] R. Leitgeb, C. Hitzenberger, and A. Fercher, “Performance of fourier domain vs. time domain optical coherence tomography,” *Opt. Express* **11**, 889–894 (2003). URL <http://www.opticsexpress.org/abstract.cfm?URI=oe-11-8-889>.
- [3] J. F. de Boer, B. Cense, B. H. Park, M. C. Pierce, G. J. Tearney, and B. E. Bouma, “Improved signal-to-noise ratio in spectral-domain compared with time-domain optical coherence tomography,” *Opt. Lett.* **28**, 2067–2069 (2003).
- [4] M. Choma, M. Sarunic, C. Yang, and J. Izatt, “Sensitivity advantage of swept source and Fourier domain optical coherence tomography,” *Opt. Express* **11**, 2183–2189 (2003). URL <http://www.opticsexpress.org/abstract.cfm?URI=oe-11-18-2183>.
- [5] M. Wojtkowski, T. Bajraszewski, P. Targowski, and A. Kowalczyk, “Real-time in vivo imaging by high-speed spectral optical coherence tomography,” *Opt. Lett.* **28**, 1745–1747 (2003).
- [6] N. Nassif, B. Cense, B. H. Park, S. H. Yun, T. C. Chen, B. E. Bouma, G. J. Tearney, and J. F. de Boer, “In vivo human retinal imaging by ultrahigh-speed spectral domain optical coherence tomography,” *Opt. Lett.* **29**, 480–482 (2004).
- [7] S. Yun, G. Tearney, J. de Boer, N. Iftimia, and B. Bouma, “High-speed optical frequency-domain imaging,” *Opt. Express* **11**, 2953–2963 (2003). URL <http://www.opticsexpress.org/abstract.cfm?URI=oe-11-22-2953>.
- [8] S. Yun, G. Tearney, B. Bouma, B. Park, and J. de Boer, “High-speed spectral-domain optical coherence tomography at 1.3 μm wavelength,” *Opt. Express* **11**, 3598–3604 (2003). URL <http://www.opticsexpress.org/abstract.cfm?URI=oe-11-26-3598>.
- [9] R. Huber, D. C. Adler, and J. G. Fujimoto, “Buffered Fourier domain mode locking: unidirectional swept laser sources for optical coherence tomography imaging at 370,000 lines/s,” *Opt. Lett.* **31**, 2975–2977 (2006).

- [10] M. R. Hee, D. Huang, E. A. Swanson, and J. G. Fujimoto, “Polarization-sensitive low-coherence reflectometer for birefringence characterization and ranging,” *J. Opt. Soc. Am. B* **9**, 903–908 (1992).
- [11] J. F. de Boer, T. E. Milner, M. J. C. van Gemert, and J. S. Nelson, “Two-dimensional birefringence imaging in biological tissue by polarization-sensitive optical coherence tomography,” *Opt. Lett.* **22**, 934–936 (1997).
- [12] M. G. Ducros, J. F. de Boer, H. Huang, L. C. Chao, Z. Chen, J. S. Nelson, T. E. Milner, and I. H. G. Rylander, “Polarization sensitive optical coherence tomography of the rabbit eye,” *IEEE J. Sel. Top. Quantum Electron.* **5**, 1159–1167 (1999).
- [13] M. G. Ducros, J. D. Marsack, H. G. R. III, S. L. Thomsen, and T. E. Milner, “Primate retina imaging with polarization-sensitive optical coherence tomography,” *J. Opt. Soc. Am. A* **18**, 2945–2956 (2001).
- [14] B. Cense, T. C. Chen, B. H. Park, M. C. Pierce, and J. F. de Boer, “Thickness and birefringence of healthy retinal nerve fiber layer tissue measured with polarization-sensitive optical coherence tomography,” *Invest. Ophthalmol. Vis. Sci.* **45**, 2606–2612 (2004).
- [15] B. Cense, T. C. Chen, B. H. Park, M. C. Pierce, and J. F. de Boer, “*In vivo* birefringence and thickness measurements of the human retinal nerve fiber layer using polarization-sensitive optical coherence tomography,” *J. Biomed. Opt.* **9**, 121–125 (2004).
- [16] E. Götzinger, M. Pircher, and C. K. Hitzenberger, “High speed spectral domain polarization sensitive optical coherence tomography of the human retina,” *Opt. Express* **13**, 10,217–10,229 (2005). URL <http://www.opticsexpress.org/abstract.cfm?URI=oe-13-25-10217>.
- [17] N. J. Kemp, J. Park, H. N. Zaatari, H. G. Rylander, and T. E. Milner, “High-sensitivity determination of birefringence in turbid media with enhanced polarization-sensitive optical coherence tomography,” *J. Opt. Soc. Am. A* **22**, 552–560 (2005).
- [18] J. F. de Boer, S. M. Srinivas, A. Malekafzali, Z. Chen, and J. S. Nelson, “Imaging thermally damaged tissue by polarization sensitive optical coherence tomography,” *Opt. Express* **3**, 212–218 (1998).
- [19] K. Schoenenberger, J. B. W. Colston, D. J. Maitland, L. B. D. Silva, and M. J. Everett, “Mapping of birefringence and thermal damage in tissue by use of polarization-sensitive optical coherence tomography,” *Appl. Opt.* **37**, 6026–6036 (1998).
- [20] B. H. Park, C. Saxer, S. M. Srinivas, J. S. Nelson, and J. F. de Boer, “*In vivo* burn depth determination by high-speed fiber-based polarization sensitive optical coherence tomography,” *J. Biomed. Opt.* **6**, 474–479 (2001).

- [21] S. Jiao and L. V. Wang, "Jones-matrix imaging of biological tissues with quadruple-channel optical coherence tomography," *J. Biomed. Opt.* **7**, 350–358 (2002).
- [22] S. Jiao, W. Yu, G. Stoica, and L. V. Wang, "Contrast mechanisms in polarization-sensitive Mueller-matrix optical coherence tomography and application in burn imaging," *Appl. Opt.* **42**, 5191–5197 (2003).
- [23] M. C. Pierce, J. Strasswimmer, B. H. Park, B. Cense, and J. F. de Boer, "Advances in optical coherence tomography imaging for dermatology," *J. Invest. Dermatol.* **123**, 458–463 (2004).
- [24] S. M. Srinivas, J. F. de Boer, H. P. K. Keikhanzadeh, H. L. Huang, J. Zhang, W. Q. Jung, Z. Chen, and J. S. Nelson, "Determination of burn depth by polarization-sensitive optical coherence tomography," *J. Biomed. Opt.* **9**, 207–212 (2004).
- [25] W. Drexler, D. Stamper, C. Jesser, X. Li, C. Pitris, K. Saunders, S. Martin, M. B. Lodge, J. G. Fujimoto, and M. E. Brezinski, "Correlation of collagen organization with polarization sensitive imaging of in vitro cartilage: implications for osteoarthritis," *J. Rheumatol.* **28**, 1311–1318 (2001).
- [26] X. Wang, T. E. Milner, J. F. de Boer, Y. Zhang, D. H. Pashley, and J. S. Nelson, "Characterization of dentin and enamel by use of optical coherence tomography," *Appl. Opt.* **38**, 2092–2096 (1999).
- [27] A. Baumgartner, S. Dichtl, C. Hitzenberger, H. Sattmann, B. Robl, A. Moritz, A. Fercher, and W. Sperr, "Polarization-Sensitive Optical Coherence Tomography of Dental Structures," *Caries Res.* **34**, 59–69 (2000).
- [28] D. Fried, J. Xie, S. Shafi, J. D. B. Featherstone, T. M. Breunig, and C. Le, "Imaging caries lesions and lesion progression with polarization sensitive optical coherence tomography," *J. Biomed. Opt.* **7**, 618–627 (2002).
- [29] Y. Chen, L. Otis, D. Piao, and Q. Zhu, "Characterization of dentin, enamel, and carious lesions by a polarization-sensitive optical coherence tomography system," *Appl. Opt.* **44**, 2041–2048 (2005).
- [30] R. S. Jones, C. L. Darling, J. D. B. Featherstone, and D. Fried, "Remineralization of in vitro dental caries assessed with polarization-sensitive optical coherence tomography," *J. Biomed. Opt.* **11**, 014,016 (2006).
- [31] J. J. Pasquesi, S. C. Schlachter, M. D. Boppart, E. Chaney, S. J. Kaufman, and S. A. Boppart, "*In vivo* detection of exercised-induced ultrastructural changes in genetically-altered murine skeletal muscle using polarization-sensitive optical coherence tomography," *Opt. Express* **14**, 1547–1556 (2006). URL <http://www.opticsexpress.org/abstract.cfm?URI=oe-14-4-1547>.

- [32] C. Hitzenberger, E. Goetzinger, M. Sticker, M. Pircher, and A. Fercher, “Measurement and imaging of birefringence and optic axis orientation by phase resolved polarization sensitive optical coherence tomography,” *Opt. Express* **9**, 780–790 (2001). URL <http://www.opticsexpress.org/abstract.cfm?URI=oe-9-13-780>.
- [33] G. Yao and L. V. Wang, “Two-dimensional depth-resolved Mueller matrix characterization of biological tissue by optical coherence tomography,” *Opt. Lett.* **24**, 537–539 (1999).
- [34] S. Jiao and L. V. Wang, “Two-dimensional depth-resolved Mueller matrix of biological tissue measured with double-beam polarization-sensitive optical coherence tomography,” *Opt. Lett.* **27**, 101–103 (2002).
- [35] Y. Yasuno, S. Makita, Y. Sutoh, M. Itoh, and T. Yatagai, “Birefringence imaging of human skin by polarization-sensitive spectral interferometric optical coherence tomography,” *Opt. Lett.* **27**, 1803–1805 (2002).
- [36] Y. Yasuno, S. Makita, T. Endo, M. Itoh, T. Yatagai, M. Takahashi, C. Katada, and M. Mutoh, “Polarization-sensitive complex Fourier domain optical coherence tomography for Jones matrix imaging of biological samples,” *Appl. Phys. Lett.* **85**, 3023–3025 (2004).
- [37] C. E. Saxer, J. F. de Boer, B. H. Park, Y. Zhao, Z. Chen, and J. S. Nelson, “High-speed fiber based polarization-sensitive optical coherence tomography of in vivo human skin,” *Opt. Lett.* **25**, 1355–1357 (2000).
- [38] J. E. Roth, J. A. Kozak, S. Yazdanfar, A. M. Rollins, and J. A. Izatt, “Simplified method for polarization-sensitive optical coherence tomography,” *Opt. Lett.* **26**, 1069–1071 (2001).
- [39] B. H. Park, M. C. Pierce, B. Cense, and J. F. de Boer, “Jones matrix analysis for a polarization-sensitive optical coherence tomography system using fiber-optic components,” *Opt. Lett.* **29**, 2512–2514 (2004).
- [40] S. Jiao, W. Yu, G. Stoica, and L. V. Wang, “Optical-fiber-based Mueller optical coherence tomography,” *Opt. Lett.* **28**, 1206–1208 (2003).
- [41] S. Jiao, M. Todorović, G. Stoica, and L. V. Wang, “Fiber-based polarization-sensitive Mueller matrix optical coherence tomography with continuous source polarization modulation,” *Appl. Opt.* **44**, 5463–5467 (2005).
- [42] J. Zhang, W. Jung, J. Nelson, and Z. Chen, “Full range polarization-sensitive Fourier domain optical coherence tomography,” *Opt. Express* **12**, 6033–6039 (2004). URL <http://www.opticsexpress.org/abstract.cfm?URI=oe-12-24-6033>.
- [43] B. Park, M. C. Pierce, B. Cense, S.-H. Yun, M. Mujat, G. Tearney, B. Bouma, and J. de Boer, “Real-time fiber-based multi-functional spectral-domain optical

- coherence tomography at 1.3 μm ,” *Opt. Express* **13**, 3931–3944 (2005). URL <http://www.opticsexpress.org/abstract.cfm?URI=oe-13-11-3931>.
- [44] B. Cense, “Optical coherence tomography for retinal imaging,” Ph.D. thesis, Twente University (2005).
- [45] M. Yamanari, S. Makita, V. D. Madjarova, T. Yatagai, and Y. Yasuno, “Fiber-based polarization-sensitive Fourier domain optical coherence tomography using B-scan-oriented polarization modulation method,” *Opt. Express* **14**, 6502–6515 (2006). URL <http://www.opticsexpress.org/abstract.cfm?URI=oe-14-14-6502>.
- [46] W. Oh, S. Yun, B. Vakoc, M. Shishkov, A. Desjardins, B. Park, J. de Boer, G. Tearney, and B. Bouma, “High-speed polarization sensitive optical frequency domain imaging with frequency multiplexing,” *Opt. Express* **16**, 1096–1103 (2008). URL <http://www.opticsexpress.org/abstract.cfm?URI=oe-16-2-1096>.
- [47] J. F. de Boer, T. E. Milner, and J. S. Nelson, “Determination of the depth-resolved Stokes parameters of light backscattered from turbid media by use of polarization-sensitive optical coherence tomography,” *Opt. Lett.* **24**, 300–302 (1999).
- [48] M. Zhao, Y. K. Tao, and J. A. Izatt, “High-Speed Fiber-Based Polarization Sensitive Retinal SDOCT,” *Invest. Ophthalmol. Vis. Sci.* **48**(5), 2615– (2007).
- [49] M. Wojtkowski, V. J. Srinivasan, T. H. Ko, J. G. Fujimoto, A. Kowalczyk, and J. S. Duker, “Ultrahigh-resolution, high-speed, Fourier domain optical coherence tomography and methods for dispersion compensation,” *Opt. Express* **12**, 2404–2422 (2004).
- [50] B. H. Park, M. C. Pierce, B. Cense, and J. F. de Boer, “Optic axis determination accuracy for fiber-based polarization-sensitive optical coherence tomography,” *Opt. Lett.* **30**, 2587–2589 (2005).
- [51] M. C. Pierce, M. Shishkov, B. H. Park, N. A. Nassif, B. E. Bouma, G. J. Tearney, and J. F. de Boer, “Effects of sample arm motion in endoscopic polarization-sensitive optical coherence tomography,” *Opt. Express* **13**, 5739–5749 (2005).
- [52] B. R. White, M. C. Pierce, N. Nassif, B. Cense, B. H. Park, G. J. Tearney, B. E. Bouma, T. C. Chen, and J. F. de Boer, “*In vivo* dynamic human retinal blood flow imaging using ultra-high-speed spectral domain optical coherence tomography,” *Opt. Express* **11**, 3490–3497 (2003).
- [53] M. Todorović, S. Jiao, L. V. Wang, and G. Stoica, “Determination of local polarization properties of biological samples in the presence of diattenuation by use of Mueller optical coherence tomography,” *Opt. Lett.* **29**, 2402–2404 (2004).

- [54] M. C. Pierce, J. Strasswimmer, B. H. Park, B. Cense, and J. F. de Boer, “Birefringence measurements in human skin using polarization-sensitive optical coherence tomography,” *J. Biomed. opt.* **9**, 287–291 (2004).
- [55] M. Pircher, E. Goetzinger, R. Leitgeb, and C. Hitzenberger, “Three dimensional polarization sensitive OCT of human skin in vivo,” *Opt. Express* **12**, 3236–3244 (2004). URL <http://www.opticsexpress.org/abstract.cfm?URI=oe-12-14-3236>.
- [56] H. A. Quigley, E. M. Addicks, and W. R. Green, “Optic nerve damage in human glaucoma. III. Quantitative correlation of nerve fiber loss and visual field defect in glaucoma, ischemic neuropathy, papilledema, and toxic neuropathy,” *Arch. Ophthalmol* **100**, 135–146 (1982).
- [57] J. S. Schuman, M. R. Hee, C. A. Puliafito, C. Wong, T. Pedut-Kloizman, C. P. Lin, E. Hertzmark, J. A. Izatt, E. A. Swanson, and J. G. Fujimoto, “Quantification of nerve fiber layer thickness in normal and glaucomatous eyes using optical coherence tomography,” *Arch. Ophthalmol.* **113**, 586–596 (1995).
- [58] R. N. Weinreb, A. W. Dreher, A. Coleman, H. Quigley, B. Shaw, and K. Reiter, “Histopathologic validation of Fourier-ellipsometry measurements of retinal nerve fiber layer thickness,” *Arch. Ophthalmol.* **108**, 557–560 (1990).
- [59] A. W. Dreher, K. Reiter, and R. N. Weinreb, “Spatially resolved birefringence of the retinal nerve fiber layer assessed with a retinal laser ellipsometer,” *Appl. Opt.* **31**, 3730–3735 (1992).
- [60] Q. Zhou and R. N. Weinreb, “Individualized compensation of anterior segment birefringence during scanning laser polarimetry,” *Invest. Ophthalmol. Vis. Sci.* **43**, 2221–2228 (2002).
- [61] B. Cense, T. C. Chen, B. H. Park, M. C. Pierce, and J. F. de Boer, “*In vivo* depth-resolved birefringence measurements of the human retinal nerve fiber layer by polarization-sensitive optical coherence tomography,” *Opt. Lett.* **27**, 1610–1612 (2002).
- [62] M. Pircher, E. Gotzinger, O. Findl, S. Michels, W. Geitzenauer, C. Leydolt, U. Schmidt-Erfurth, and C. K. Hitzenberger, “Human Macula Investigated In Vivo with Polarization-Sensitive Optical Coherence Tomography,” *Invest. Ophthalmol. Vis. Sci.* **47**, 5487–5494 (2006). URL <http://www.iovs.org/cgi/content/abstract/47/12/5487>.
- [63] B. Cense, M. Mujat, T. C. Chen, B. H. Park, and J. F. de Boer, “Polarization-sensitive spectral-domain optical coherence tomography using a single line scan camera,” *Opt. Express* **15**, 2421–2431 (2007). URL <http://www.opticsexpress.org/abstract.cfm?URI=oe-15-5-2421>.

- [64] M. Mujat, B. H. Park, B. Cense, T. C. Chen, and J. F. de Boer, “Autocalibration of spectral-domain optical coherence tomography spectrometers for in vivo quantitative retinal nerve fiber layer birefringence determination,” *Journal of Biomedical Optics* **12**, 041205 (pages 6) (2007).
- [65] H. Bagga, D. S. Greenfield, W. Feuer, and R. W. Knighton, “Scanning laser polarimetry with variable corneal compensation and optical coherence tomography in normal and glaucomatous eyes,” *Am. J. Ophthalmol.* **135**, 521–529 (2003).
- [66] N. J. Reus, T. P. Colen, and H. G. Lemij, “Visualization of localized retinal nerve fiber layer defects with the GDx with individualized and with fixed compensation of anterior segment birefringence,” *Ophthalmol.* **110**, 1512–1516 (2003).
- [67] N. J. Reus and H. G. Lemij, “The relationship between standard automated perimetry and GDx VCC measurements,” *Invest. Ophthalmol. Vis. Sci.* **45**, 840–845 (2004).
- [68] X.-R. Huang, H. Bagga, D. S. Greenfield, and R. W. Knighton, “Variation of peripapillary retinal nerve fiber layer birefringence in normal human subjects,” *Invest. Ophthalmol. Vis. Sci.* **45**, 3073–3080 (2004).
- [69] M. Wojtkowski, V. Srinivasan, J. G. Fujimoto, T. Ko, J. S. Schuman, A. Kowalczyk, and J. S. Duker, “Three-dimensional retinal imaging with high-speed ultrahigh-resolution optical coherence tomography,” *Ophthalmol.* **112**, 1734–1746 (2005).
- [70] S. Makita, Y. Hong, M. Yamanari, T. Yatagai, and Y. Yasuno, “Optical coherence angiography,” *Opt. Express* **14**, 7821–7840 (2006). URL <http://www.opticsexpress.org/abstract.cfm?URI=oe-14-17-7821>.
- [71] Q. Zhou, J. Reed, R. Betts, P. Trost, P.-W. Lo, C. Wallace, R. Bienias, G. Li, R. Winnick, W. Papworth, and M. Sinai, “Detection of glaucomatous retinal nerve fiber layer damage by scanning laser polarimetry with variable corneal compensation,” *Proc. SPIE* **4951**, 32–41 (2003).
- [72] M. Yamanari, M. Miura, S. Makita, T. Yatagai, and Y. Yasuno, “Retinal birefringence measurement with polarization sensitive Fourier domain optical coherence tomography,” *Invest. Ophthalmol. Vis. Sci.* **47**, E–Abstract 3309 (2006).
- [73] M. Yamanari, M. Miura, S. Makita, T. Yatagai, and Y. Yasuno, “Birefringence measurement of retinal nerve fiber layer using polarization-sensitive spectral domain optical coherence tomography with Jones matrix based analysis,” *Proc. of SPIE* **6429**, 64,292M (2007).
- [74] Y. Yasuno, V. D. Madjarova, S. Makita, M. Akiba, A. Morosawa, C. Chong, T. Sakai, K.-P. Chan, M. Itoh, and T. Yatagai, “Three-dimensional and high-speed swept-source optical coherence tomography for in vivo investigation of

- human anterior eye segments,” *Opt. Express* **13**, 10,652–10,664 (2005). URL <http://www.opticsexpress.org/abstract.cfm?URI=oe-13-26-10652>.
- [75] B. Vakoc, S. Yun, J. de Boer, G. Tearney, and B. Bouma, “Phase-resolved optical frequency domain imaging,” *Opt. Express* **13**, 5483–5493 (2005). URL <http://www.opticsexpress.org/abstract.cfm?URI=oe-13-14-5483>.
- [76] J. Zhang and Z. Chen, “In vivo blood flow imaging by a swept laser source based Fourier domain optical Doppler tomography,” *Opt. Express* **13**, 7449–7457 (2005). URL <http://www.opticsexpress.org/abstract.cfm?URI=oe-13-19-7449>.
- [77] M. Pircher, E. Goetzinger, R. Leitgeb, and C. K. Hitzenberger, “Transversal phase resolved polarization sensitive optical coherence tomography,” *Phys. Med. Biol.* **49**, 1257–1263 (2004).
- [78] Y. Chen, D. M. de Bruin, C. Kerbage, and J. F. de Boer, “Spectrally balanced detection for optical frequency domain imaging,” *Opt. Express* **15**, 16,390–16,399 (2007). URL <http://www.opticsexpress.org/abstract.cfm?URI=oe-15-25-16390>.
- [79] M. Miura, M. Yamanari, T. Iwasaki, A. E. Elsner, S. Makita, T. Yatagai, and Y. Yasuno, “Imaging polarimetry in age-related macular degeneration,” *Invest. Ophthalmol. Vis. Sci.* (2008). Accepted for publication.
- [80] S. Sakai, M. Yamanari, A. Miyazawa, M. Matsumoto, N. Nakagawa, K. Kawabata, T. Yatagai, and Y. Yasuno, “In vivo three-dimensional birefringence analysis shows collagen differences between young and old photo-aged human skin,” *J. Invest. Dermatol.* (2008). Accepted for publication.

Acknowledgements

I would like to thank all members in our laboratory for their help. Yasuno-san pushed me towards the research field of PS-OCT. He has always provided me with the best opportunity and resources for my research. Makita-san built our high-speed SD-OCT and the sophisticated code, which is applied to the PS-SD-OCT system. Without their help, I could not build the PS-OCT systems.

I am grateful to all the committee members, Prof. Masahide Itoh, Prof. Sadao Aoki, Prof. Katsumi Kose, Prof. Tetsuro Ohshika, Prof. Toshiaki Iwai, and Prof. Masahiro Miura. Prof. Itoh was an official adviser for me, and he has supported me for six years in my bachelor, master and PhD courses. Prof. Toyohiko Yatagai also supported me from my bachelor's work to present, even though he is now in Utsunomiya University. I thank Prof. Ohshika and Prof. Keisuke Kawana for their support of my work on the anterior eye segment. I am also grateful to Prof. Miura and Prof. Ann E. Elsner for the collaboration on the AMD measurement. I believe that the wonderful meeting with Prof. Miura, when I was building the PS-SD-OCT system, was a miracle. I thank Dr. Shingo Sakai who led the project of skin measurement by PS-OCT. I also thank Prof. Iwai, who gave me the helpful advice for my inexperienced master's work.

I thank Prof. Lihong V. Wang and all the Mueller-OCT members, especially Milōs Todorović, for fruitful discussions when I visited them for two months in the summer of 2004. This experience encouraged me to go to my PhD work.

I am grateful to Prof. Johannes F. de Boer, Dr. Boris Hyle Park, Dr. Barry Cense, Prof. Christoph Hitzenberger, and Prof. Shuliang Jiao for their kind comments and discussions in conferences. My work stands on the shoulders of their great accomplishments.

I thank my parents and my sister. They encouraged me to go to the graduate school, and they supported me from my hometown 77 km distant.

This research is supported in part by a Grant-in-aid for Scientific Research 15760026 and 18360029 from the Japan Society for the Promotion of Science (JSPS), Japan Science and Technology Agency, and the Special Research Project of Nanoscience at the University of Tsukuba. The author was supported in part by JSPS through a contract under the Promotion of Creative Interdisciplinary Materials Science for Novel Functions, 21st Century Center of Excellence (COE) Program.

Curriculum vitae

1999-2003 College of Engineering Sciences, University of Tsukuba
March 2003 B. S. in Engineering, University of Tsukuba
2003-2005 Institute of Applied Physics, University of Tsukuba
March 2005 M. S. in Engineering, University of Tsukuba
2005-present Institute of Applied Physics, University of Tsukuba

Masahiro Yamanari was born on February 16, 1981 in Ibaraki, Japan. He received B. S. in Engineering in 2003 and M. S. in Engineering in 2005 from University of Tsukuba. In 2005 he started his PhD work in University of Tsukuba, which focused on the development of polarization-sensitive optical coherence tomography.

Publications

As a first author

1. M. Yamanari, Y. Yasuno, T. Yatagai, and M. Itoh, "Analysis of the polarization dependence of multiple backscattering light from red blood cell suspensions," *Optics (Kogaku in Japanese)* **34**, 90–96, 2005.
2. M. Yamanari, S. Makita, V. D. Madjarova, T. Yatagai, and Y. Yasuno, "Fiber-based polarization-sensitive Fourier domain optical coherence tomography using B-scan-oriented polarization modulation method," *Opt. Express* **14**, 6502–6515 (2006).
3. M. Yamanari, M. Miura, S. Makita, T. Yatagai, and Y. Yasuno, "Phase retardation measurement of retinal nerve fiber layer by polarization-sensitive spectral-domain optical coherence tomography and scanning laser polarimetry," *J. Biomed. Opt.* **13**, 2008, to be published.

As a coauthor

4. M. Itoh, M. Yamanari, Y. Yasuno, and T. Yatagai, "Polarization characteristics of multiple backscattering in human blood cell suspensions," *Optical and Quantum Electronics* **37**, 1277-1285, 2005.

5. Y. Hori, Y. Yasuno, S. Sakai, M. Matsumoto, T. Sugawara, V. D. Madjarova, M. Yamanari, S. Makita, T. Araki, M. Itoh, and T. Yatagai, "Automatic characterization and segmentation of human skin using three-dimensional optical coherence tomography," *Opt. Express* **14**, 1862–1877, 2006.
6. S. Makita, Y. Hong, M. Yamanari, T. Yatagai, Y. Yasuno, "Optical coherence angiography," *Opt. Express* **14**, 7821–7840, 2006.
7. Y. Yasuno, Y. Hong, S. Makita, M. Yamanari, M. Akiba, M. Miura, T. Yatagai, "In vivo high-contrast imaging of deep posterior eye by 1-um swept source optical coherence tomography and scattering optical coherence angiography," *Opt. Express* **15**, 6121–6139, 2007.
8. Y. Hong, S. Makita, M. Yamanari, M. Miura, S. Kim, T. Yatagai, Y. Yasuno, "Three-dimensional visualization of choroidal vessels by using standard and ultra-high resolution scattering optical coherence angiography," *Opt. Express* **15**, 7538–7550, 2007.
9. Y. Nakamura, S. Makita, M. Yamanari, M. Itoh, T. Yatagai, Y. Yasuno, "High-speed three-dimensional human retinal imaging by line-field spectral domain optical coherence tomography," *Opt. Express* **15**, 7103–7116, 2007.
10. S. Sakai, M. Yamanari, A. Miyazawa, M. Matsumoto, N. Nakagawa, K. Kawabata, T. Yatagai, Y. Yasuno, "In vivo three-dimensional birefringence analysis shows collagen differences between young and old photo-aged human skin," *J. Invest. Dermatol.*, accepted for publication, January 2008.
11. M. Miura, M. Yamanari, T. Iwasaki, A. E. Elsner, S. Makita, T. Yatagai, Y. Yasuno, "Imaging polarimetry in age-related macular degeneration," *Invest. Ophthalmol. Vis. Sci.*, accepted for publication, February 2008.

Conference proceedings

1. M. Yamanari, Y. Yasuno, S. Makita, Y. Nakamura, Y. Hori, M. Itoh, and T. Yatagai, "Polarization sensitive Fourier domain optical coherence tomography with continuous polarization modulation," *Proc. SPIE* **6079**, 60792A, 2006.
2. M. Yamanari, M. Miura, S. Makita, T. Yatagai, Y. Yasuno, "Birefringence measurement of retinal nerve fiber layer using polarization-sensitive spectral domain optical coherence tomography with Jones matrix based analysis," *Proc. SPIE* **6429**, 64292M, 2007.
3. M. Yamanari, M. Miura, S. Makita, T. Yatagai, Y. Yasuno, "Phase retardation measurement of retinal nerve fiber layer using polarization-sensitive spectral domain optical coherence tomography and scanning laser polarimetry," *Proc. SPIE* **6627**, 66270I, 2007.

Conferences

Oral presentations in domestic conferences

1. 山成正宏, 安野嘉晃, 伊藤雅英, 谷田貝豊彦, “Monte Carlo 法によるポリスチレン球懸濁液からの後方散乱光の偏光特性の解析,” 第 64 回応用物理学学会学術講演会, 31p-Q-3, 福岡大学, August 2003.
2. 山成正宏, 安野嘉晃, 谷田貝豊彦, 伊藤雅英, “赤血球による後方多重散乱光の偏光依存性の解析,” 第 51 回応用物理学関係連合講演会, 28a-K-6, 東京工科大学, March 2004.
3. 山成正宏, 安野嘉晃, 巻田修一, 中村佳史, 堀 泰明, Violeta Madjarova, 青木剛毅, 伊藤雅英, 谷田貝豊彦, “ビデオレート偏光感受型フーリエドメイン OCT による生体複屈折の計測,” 第 66 回応用物理学学会学術講演会, 10a-ZE-10, 徳島大学, September 2005.
4. 山成正宏, 安野嘉晃, 巻田修一, 中村佳史, 伊藤雅英, 谷田貝豊彦, “連続入射偏光変調による偏光感受型フーリエドメイン光コヒーレンストモグラフィー,” Optics Japan, 24pE2, 学術総合センター, November 2005.
5. 山成正宏, 巻田修一, 谷田貝豊彦, 安野嘉晃, “偏光感受型フーリエドメイン OCT を用いた生体の繊維状組織の 3 次元計測,” 第 67 回応用物理学学会学術講演会, 29p-S-1, 立命館大学, August 2006.
6. 山成正宏, 巻田修一, 三浦雅博, 安野嘉晃, “偏光感受型 swept-source optical coherence tomography,” Optics and Photonics Japan, 27pE6, Osaka, November 2007.

Oral presentations in international conferences

1. M. Yamanari, Y. Yasuno, T. Yatagai, and M. Itoh, “Analysis of the polarization dependence of multiple backscattering light from red blood cells,” Photonics West, 5695-11, San Jose, California, USA, January 2005.
2. M. Yamanari, Y. Yasuno, S. Makita, Y. Nakamura, Y. Hori, M. Itoh, T. Yatagai, “Polarization sensitive Fourier domain optical coherence tomography with continuous polarization modulation,” Photonics West, 6079-57, San Jose, California, USA, January 2006.
3. M. Yamanari, M. Miura, S. Makita, T. Yatagai, Y. Yasuno, “Phase retardation measurement of retinal nerve fiber layer using polarization-sensitive spectral domain optical coherence tomography and scanning laser polarimetry,” European Conferences on Biomedical Optics, 6627-16, Munich, Germany, June 2007.
4. M. Yamanari, S. Makita, T. Yatagai, Y. Yasuno, “Polarization-sensitive swept-source optical coherence tomography with continuous polarization modulation,” Photonics West, 6847-55, San Jose, California, USA, January 2008.

Poster presentations in international conferences

1. M. Yamanari, Y. Yasuno, S. Makita, Y. Hong, Y. Nakamura, V. D. Madjarova, M. Itoh, T. Yatagai, "Retinal Birefringence Measurement With Polarization Sensitive Fourier Domain Optical Coherence Tomography," ARVO annual meeting, Program #3309, Poster # B842, Fort Lauderdale, Florida, USA, May 2006.
2. M. Yamanari, M. Miura, S. Makita, T. Yatagai, Y. Yasuno, "Birefringence measurement of retinal nerve fiber layer using polarization-sensitive spectral domain optical coherence tomography with Jones matrix based analysis," Photonics West, 6429-93, San Jose, California, USA, January 2007.
3. M. Yamanari, M. Miura, S. Makita, T. Yatagai, Y. Yasuno, "Birefringence measurement of retinal nerve fiber layer by polarization-sensitive spectral domain optical coherence tomography and the comparison with scanning laser polarimetry," ARVO annual meeting, Program #505, Poster #B799, Fort Lauderdale, Florida, USA, May 2007.
4. M. Yamanari, M. Miura, S. Makita, T. Yatagai, Y. Yasuno, "Quantitative comparison of phase retardation measured by polarization-sensitive spectral-domain optical coherence tomography and scanning laser polarimetry," CLEO Pacific Rim, ThP_053, Seoul, Korea, August 2007.